Two-Qutrit Quantum Algorithms on a Programmable Superconducting Processor

Tanay Roy, Ziqian Li, Eliot Kapit, and DavidI. Schuster

Phys. Rev. Applied **19**, 064024 — Published 7 June 2023

DOI: 10.1103/PhysRevApplied.19.064024

Two-qutrit quantum algorithms on a programmable superconducting processor

Tanay Roy,[1,2,*] Ziqian Li,[1,2,*] Eliot Kapit,[3] and David I. Schuster[1,2,4,†]

[1] *James Franck Institute, University of Chicago, Chicago, Illinois 60637, USA*
[2] *Department of Physics, University of Chicago, Chicago, Illinois 60637, USA*
[3] *Department of Physics, Colorado School of Mines, Golden, CO 80401*
[4] *Pritzker School of Molecular Engineering, University of Chicago, Chicago, Illinois 60637, USA*

(Dated: May 9, 2023)

Processing quantum information using quantum three-level systems or qutrits as the fundamental unit is an alternative to contemporary qubit-based architectures with the potential to provide significant computational advantages. We demonstrate a fully programmable two-qutrit quantum processor by utilizing the third energy eigenstates of two transmons. We develop a parametric coupler to achieve excellent connectivity in the nine-dimensional Hilbert space enabling efficient implementations of two-qutrit gates. We characterize our processor by realizing several algorithms like Deutsch-Jozsa, Bernstein-Vazirani, and Grover's search. Our hardware efficient protocols allow us to show that two stages of Grover's amplification can improve the success rates of an unstructured search with quantum advantage. Our results pave the way for building fully programmable ternary quantum processors using transmons as building blocks for a universal quantum computer.

I. INTRODUCTION

Noisy intermediate-scale quantum (NISQ) computers [1] are making rapid progress toward practical applications with demonstrated advantage over classical algorithms for specific problems [2, 3]. However, a majority of those processors utilize quantum two-level systems. Processing information using d-dimensional quantum systems or qudits can boost performance through access to a larger computational space and with fewer entangling gates for certain algorithms [4–8]. In the family of qudits, quantum three-level systems or qutrits are the closest members to qubits and provide the immediate opportunity to explore possibilities beyond two levels as basic units.

Theoretical studies show that qutrit-based processors can be beneficial for quantum error correction by providing compact logical encoding to protect against erasure [9, 10] and ternary errors [11], enhance fault tolerance [12], enable magic state distillation [13] and efficient decomposition of multi-qubit gates [14]. Other proposals claim improved implementations of quantum gates [15], algorithms [16], simulations [17], cryptography [18, 19], and communication [20] using qutrits. Due to these advantages, several platforms including photonic circuits [21, 22], trapped ions [23, 24], nitrogen-vacancy centers [25], and superconducting circuits [26–29] have started to explore qutrits as computational units. In the superconducting circuits platform [30], the transmon [31] is a natural choice to be utilized as a qutrit due to its fast gates [26, 28], long coherence times [32, 33], weak anharmonicity, and easy measurement [34]. While a significant effort is being made in realizing efficient two-qutrit gates [26–28] with demonstrations of solving specific problems [35], implementing multiple generic quantum algorithms on a single processor has remained a challenge in the circuit QED architecture [30] due to limitations arising from decoherence, slow, static inter-qutrit interaction or native entangling operations restricted to a smaller subspace.

In this work, we present a versatile two-qutrit processor with excellent connectivity between different states of the full Hilbert space facilitating a rich set of native entangling gates. The connectivity is achieved through multiple beam-splitting and two-photon squeezing-like primitive operations enabled by a linear parametric coupler [36, 37]. We demonstrate two-qutrit versions of Deutsch-Jozsa [38, 39], Bernstein-Vazirani [39, 40], and Grover's search [41] algorithms without using any auxiliary qutrit (ancilla) [42]. Deutsch-Jozsa and Bernstein-Vazirani algorithms provide exponential and linear speed-ups respectively over corresponding classical algorithms, whereas Grover's search provides a quadratic improvement. We perform two stages of Grover's amplification with success probabilities significantly larger than classically achievable values. To our knowledge, ours is the *first successful demonstration* of a qutrit-based Grover's search across any quantum computing platform.

II. METHODS

A. Device description

Our two-qutrit processor, shown in Fig. 1(a), is comprised of two transmons [31] (Q_1 and Q_2), each having its readout resonator. Parametric coupling [36] between the two transmons is realized by grounding the transmon junctions [37] through a superconducting quantum interference device (SQUID). The SQUID acts as a tunable inductor when an external DC magnetic field Φ_{ext} is threaded into the loop. The transmon pads are also

* Equal contribution
† Present address: Department of Applied Physics, Stanford University, Stanford, California 94305, USA

designed to provide a static capacitive coupling with a strength larger than the inductive coupling at zero external flux. By applying a finite $\Phi_{\rm ext}$ one can, thus, nullify the competing capacitive and inductive energies to minimize the cross-Kerr coupling. The fast-flux line is used to enable various inter-qutrit interactions by modulating the SQUID at appropriate radio frequencies, whereas the charge lines can be utilized to drive qutrit-resonator sidebands. Individual manipulation of the qutrits are done by sending appropriate microwave pulses to the resonators, and the states of the qutrits are determined through transmission measurements. We keep large Josephson-to-charging energy ratios ($\gtrsim 90$) to maintain long dephasing times for the second excited states ($|2\rangle$) for both transmons [31]. Figure 1(b) shows the equivalent circuit diagram.

B. Hamiltonian and operating point

The system can be described by the following Hamiltonian when no parametric drives are present

$$\frac{H_{\rm sys}}{\hbar} = \sum_{k=1}^{2}\left[\omega_k \hat{n}_k + \frac{\alpha_k}{2}\hat{n}_k(\hat{n}_k - 1)\right] + \sum_{j,k\geq 1} J_{jk}(\hat{n}_1)^j(\hat{n}_2)^k, \tag{1}$$

where ω_k is $|0\rangle \leftrightarrow |1\rangle$ transition frequency, α_k represents anharmonicity, and $\hat{n}_k = a_k^\dagger a_k$ is the photon number operator with $a_k^\dagger(a_k)$ being the creation (annihilation) operator for the k-th qutrit. For our device, $\omega_k/2\pi = \{3.3494, 3.8310\}$ GHz and $\alpha_k/2\pi = \{-115.2, -159.8\}$ MHz for the two transmons. Figure 1(c) shows relevant energy eigenstates of Eq. (1) with the shaded area representing computational subspace and two additional levels used as auxiliary. At $\Phi_{\rm ext} = 0$, only second order parametric processes are allowed, whereas biasing the SQUID loop sufficiently away from the sweet-spot enables first order processes. The cross-Kerr couplings J_{jk} also tune with $\Phi_{\rm ext}$ and we choose a bias flux $\Phi_{\rm min}$ so that the leading order dispersive shift J_{11} is minimized. We treat $\Phi_{\rm min}$ as the coupler's 'off' point as the higher order cross-Kerr shifts J_{12} and J_{21} are very close to minimum at this bias (see Appendix C for details) ensuring reduced crosstalk during idling periods or gate operations. The value of $\Phi_{\rm min}$ is experimentally determined by performing Ramsey-fringe experiments on Q_1 conditioned on Q_2 being in the ground or first excited state and minimizing the difference in the oscillation frequencies with respect to $\Phi_{\rm ext}$.

We activate qutrit-qutrit (QQ) red and blue sidebands corresponding to photon-exchange (beam splitting) $|m,n\rangle \leftrightarrow |m-1,n+1\rangle$ and two-photon pumping (squeezing) $|m,n\rangle \leftrightarrow |m+1,n+1\rangle$ interactions respectively by modulating the SQUID at corresponding transition frequencies (see Fig. 1(c)). Here the state of the system $|m,n\rangle$ indicates the qutrits being in the energy eigenstates $|m\rangle$ and $|n\rangle$ respectively. All native entangling gates thus consist of single pulses with fixed carrier frequencies and are extremely easy to tune up (see Appendix D for details). The SQUID (coupler) mode is designed to have a frequency much larger than any relevant radio-frequency (RF) drives during the experiment at the operating point and is never populated. The blue

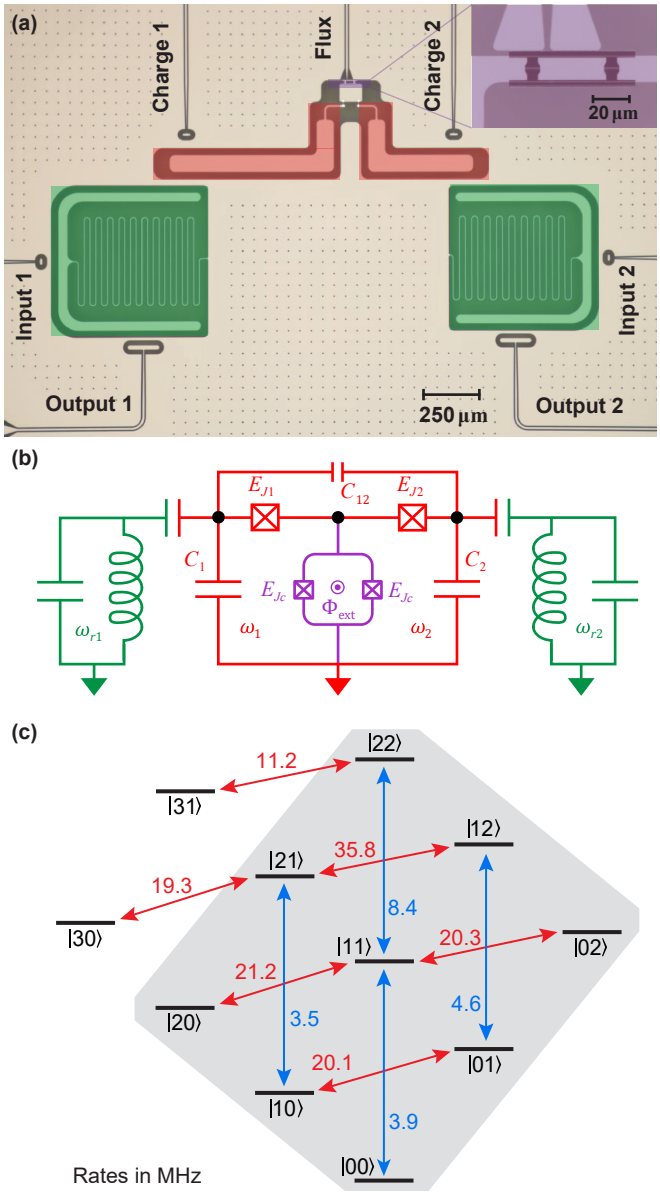

FIG. 1. The two-qutrit device. (a) False colored optical micrograph of the device. Two transmons (red) are inductively connected through a SQUID loop (purple, inset is an SEM image) that enables inter-qutrit parametric coupling. The transmons are capacitively coupled to linear resonators (green) for individual readout. Single-qutrit and readout pulses are sent through the input lines. (b) Simplified circuit diagram of the device. (c) Energy level diagram with various sideband interaction strengths (in MHz). The computational subspace is highlighted with a gray background and the other states are used as auxiliary levels to implement controlled-phase gates.

sideband frequencies (around 6.5 - 6.9 GHz) are usually one order of magnitude higher than the red sidebands (around 0.2 - 0.7 GHz). For the current geometry, stray capacitive coupling of the flux line to the SQUID [37] limits the blue sideband rates due to frequency-enhanced unwanted interactions.

C. Gate operations

Single-qutrit operations are performed by applying separate microwave pulses at $|0\rangle \leftrightarrow |1\rangle$ and $|1\rangle \leftrightarrow |2\rangle$ transition frequencies of both qutrits through the readout resonators. We use Gaussian-edge rectangular pulses having 2σ edge lengths. Single-qutrit drives use roughly 5 MHz of Rabi rates, whereas phase gates are realized by simply advancing the phases of the appropriate subsequent pulses. Consequently, the virtual phase gates take no time and are near-perfect. For the quantum algorithms we use qutrit-Hadamard H, bit-shift X (extension of the qubit's NOT gate), and qutrit-phase Z gates having the following matrix representations

$$H = \frac{1}{\sqrt{3}} \begin{bmatrix} 1 & 1 & 1 \\ 1 & \omega & \omega^2 \\ 1 & \omega^2 & \omega \end{bmatrix}, X = \begin{bmatrix} 0 & 0 & 1 \\ 1 & 0 & 0 \\ 0 & 1 & 0 \end{bmatrix}, Z = \begin{bmatrix} 1 & 0 & 0 \\ 0 & \omega & 0 \\ 0 & 0 & \omega^2 \end{bmatrix}, \tag{2}$$

where $\omega = e^{2\pi i/3}$, the cube-root of unity. Implementation of H, X, and Z gates require the application of three, two, and zero physical pulses respectively (see Appendix A).

We can implement arbitrary two-qutrit unitaries and hence achieve universal computation [43] by combining single-qutrit rotations along with generalized controlled-phase (CPhase) gates $C_\theta(\theta, |mn\rangle) = \mathcal{I} - (1 - e^{i\theta})\,|mn\rangle\langle mn|$ representing an accumulation of θ phase on the eigenstate $|mn\rangle$, where $\mathcal{I}$ is the nine-dimensional identity matrix. We realize $C_\theta(\pi, |22\rangle)$ gate by applying a 94 ns long 2π-pulse at the red sideband $|22\rangle \leftrightarrow |31\rangle$. Similarly, a 56 ns 2π-pulse at the red sideband $|21\rangle \leftrightarrow |30\rangle$ enables a $C_\theta(\pi, |21\rangle)$ gate (see Appendix D). We sandwich these C_θ gates between single-qutrit π gates to achieve phase flip on any computational basis (see Appendix E). While we have access to a native $C_\theta(\pi, |12\rangle)$ gate using the red sideband $|12\rangle \leftrightarrow |03\rangle$, we avoid that due to lower fidelity caused by significantly shorter lifetime of Q_2's $|2\rangle$ and $|3\rangle$ levels. Note that the bosonic enhancement of the coupling to an external field makes $C_\theta(\pi, |22\rangle)$ twice as fast compared to $C_\theta(\pi, |11\rangle)$ when restricting to the qubit subspace.

III. RESULTS

We implement three two-qutrit quantum algorithms on our fully programmable processor.

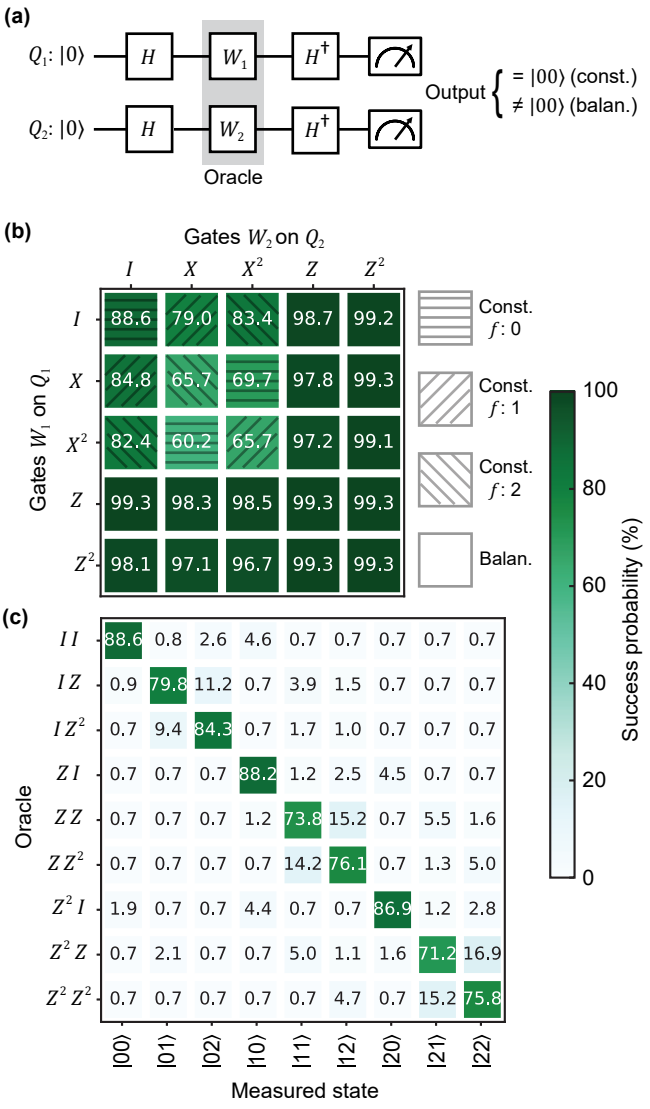

FIG. 2. Deutsch-Jozsa and Bernstein-Vazirani algorithms. (a) Quantum circuit for the algorithms. In DJ algorithm, gates $W_1, W_2 \in \{I, X, X^2, Z, Z^2\}$ are applied to implement a constant or a balanced oracle. The final output state being in $|00\rangle$ or non $|00\rangle$ distinguishes the two cases. (b) Experimental results for DJ algorithm. The rows and columns represent gates applied to Q_1 and Q_2 respectively. The average SPs are 75.5(3)% and 98.5(1)% for the constant (hatched boxes) and balanced (plain boxes) oracles respectively beating the classical rate of 50%. (c) Experimental results for BV algorithm. Each row corresponds to a specific oracle with the mapping $\{I, Z, Z^2\} \to \{0, 1, 2\}$. The diagonal terms show the SPs for all nine strings mapped to the basis states with an average of 78.3(3)%, which is much larger than the classical SP of 33.3%.

A. Deutsch-Jozsa algorithm

The Deutsch-Jozsa (DJ) algorithm [38] is one of the earliest quantum algorithms showing an exponential advantage over any classical algorithm. The original DJ algorithm applies to qubits, and here we extend it to

qutrits [39] for our quantum processor. For an n-qutrit system, the task of the DJ algorithm is to distinguish a function $f : \{0,1,2\}^n \to \{0,1,2\}$, which takes n-trits as an input and outputs one trit, between two cases, a balanced or a constant function. The constant function always results in the same output (0, 1, or 2) independent of the input, whereas the balanced function outputs each of the three possibilities for exactly one-third of the possible inputs. Note that implementing the different test functions is often termed as the *oracle*. A deterministic classical algorithm needs $3^{n-1}+1$ queries (with at least two queries in the best case) to distinguish the two cases, whereas DJ algorithm needs only one and hence provides the exponential speed-up.

Figure. 2(a) depicts our circuit implementation of the DJ algorithm. Two Hadamard gates are simultaneously applied to both qutrits initialized to $|0\rangle$ (ground state) to prepare the state $\frac{1}{3}(|0\rangle+|1\rangle+|2\rangle)^{\otimes 2}$. The oracles (gray gates in Fig. 2(a)) are implemented by applying gates (W) to the qutrits chosen from the set $\mathcal{S} = \{I, X, X^2, Z, Z^2\}$. For the constant case, W_1 and W_2 are picked up from the subset $\mathcal{S}_c = \{I, X, X^2\}$, and the total number of X gates modulo 3 specifies the constant output. For example, the gate $X \otimes X^2$ would implement constant 0, whereas $I \otimes X^2$ would be the case of constant 2. A balanced oracle can be realized by choosing any combination of elements from the set $\mathcal{S}$ except for those cases that result in a constant function. 16 different kinds of balanced functions (see Appendix G for mapping to various addition functions) are implemented in our experiment as shown in Fig. 2(a). Finally, two $H^\dagger$ gates are applied before simultaneous readout. A final measured state of $|00\rangle$ indicates a constant function, whereas any other output implies a balanced function. The theoretical success probability (SP) for each case is 100%, and the experimental results are summarized in Fig. 2(b) where the hatched (unhatched) boxes represent constant (balanced) cases. The average SPs for the three constant cases with outputs $\{0,1,2\}$ are separately 72.8(3)%, 76.5(3)% and 77.2(3)%, marked with horizontal, left and right hatching. The numbers in parentheses represent standard error of mean obtained after 20,000 repetitions of each oracle. All experimental data are corrected for measurement error (see Appendix F). For the 16 balanced cases, the average SP is 98.5(1)%. The SPs for all cases are well above the classical case, which would be 50% after a single query.

B. Bernstein-Vazirani algorithm

The Bernstein-Vazirani (BV) algorithm [40] for qutrits can be restated as follows: given an oracle $f(\boldsymbol{x}, \boldsymbol{s}) \equiv \sum_{j=1}^{n} x_j s_j \pmod 3$ that performs inner product between two strings of ternaries followed by modulo 3, the goal is to determine the unknown string $\boldsymbol{s} = \{s_1, s_2, \ldots, s_n\}$ where the user has control over the input string $\boldsymbol{x}$. The most efficient classical algorithm will need n oracle queries to find all digits of $\boldsymbol{s}$. BV algorithm, on the contrary, needs only one query and the quantum circuit is identical to the case of DJ as shown in Fig. 2(a). Oracles representing 9 different strings for our two-qutrit system are implemented by choosing gates (W) from the set $\{I, Z, Z^2\}^{\otimes 2}$ with the mapping $\{I, Z, Z^2\} \to \{0,1,2\}$. The final state of the system after measurement directly reveals the unknown string with 100% theoretical success rate. Fig. 2(c) tabulates the experimental results where the vertical axis represents gates applied to the qutrits corresponding to different unknown strings, and the horizontal axis shows the measured probability for each state. The diagonal entries indicate individual SPs for each input string mapped to the final state. The average SP for all 9 cases is 78.3(3)%, which is far above the classical SP of 33.3% after one query.

C. Grover's Search

Grover's algorithm [41] provides a quadratic speed-up for searching an unstructured database. For a database of size $\mathcal{N}$, the algorithm can find the unique input that satisfies a certain condition using $O\left(\sqrt{\mathcal{N}}\right)$ search queries, while a classical algorithm requires on average $\mathcal{N}/2$ repetitions. Several groups have recently realized Grover's search on qubit-based platforms [42, 44–47]. For the two-qutrit case with $\mathcal{N} = 3^2 = 9$, the classical SPs with one and two rounds of search are $\frac{1}{9} = 11.1\%$ and $\frac{1}{9} + \frac{8}{9}\cdot\frac{1}{8} = 22.2\%$ respectively. The corresponding theoretical SPs for the original Grover's search are 72.6% and 98.4%, and can also be modified to achieve determinism [48, 49].

The quantum circuit for the two-qutrit Grover's search is illustrated in Fig. 3(a) that doesn't use any auxiliary (ancilla) qutrit. It has four stages: initialization, oracle implementation, amplitude amplification, and measurement. Starting from the ground state, we apply Hadamard gates on both qutrits to initialize the system to the equal superposition state $\frac{1}{3}(|0\rangle+|1\rangle+|2\rangle)^{\otimes 2}$. A CPhase gate $C_\theta(\pi, |jk\rangle)$, that flips the phase of the target state $|jk\rangle$, is used to realize the oracle. Due to the structure of the Hilbert space and coherence parameters (see Fig 1(c)), we have access to two native CPhase gates $C_\theta(\pi, |22\rangle)$ and $C_\theta(\pi, |21\rangle)$ and all other CPhase gates are realized in conjunction with single-qutrit rotations (see Appendix E). Amplitude amplification of the marked state happens through the Grover's diffusion or reflection unitary, which is constructed using a phase flip of the $|22\rangle$ state sandwiched between Hadamard and Z gates. Here, we utilized the decomposition $C_\theta(\pi, |00\rangle) = (ZZ) \otimes C_\theta(\pi, |22\rangle) \otimes (Z^\dagger Z^\dagger)$. Simultaneous measurements on the qutrits are performed after one and two iterations of Grover's search for each target state. During a similar search using three qubits ($\mathcal{N} = 8$), each oracle (and amplification) step requires eight CNOT gates (for a linear chain) [46], resulting in

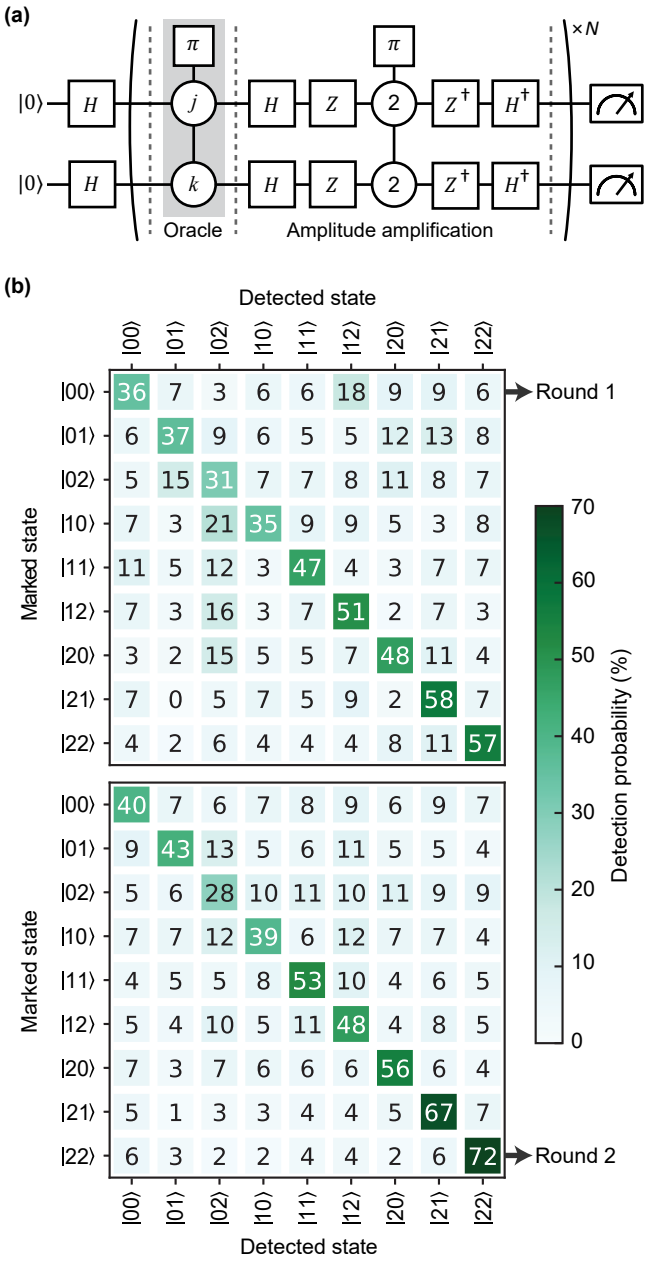

FIG. 3. Grover's search algorithm for two-qutrits. (a) Quantum circuit. The oracles are implemented by CPhase gates $C_\theta(\pi, |jk\rangle)$. The diffusion operator amplifies the detection probability of the marked state. (b) Experimental results. Detection probabilities (corrected for measurement error) after one (top panel) and two (bottom panel) rounds of amplitude amplification are obtained with 20,000 averages. All individual success rates are far beyond the corresponding classical SPs of 11.1% and 22.2%.

an *eight-fold rise* in entangling operations compared to our efficient two-qutrit implementation.

Figure 3(b) shows the experimentally obtained detection probabilities for the 9 different marked states after single (top panel) and double (bottom panel) rounds of the Grover's iteration. Each row represents a probability distribution acquired with 20,000 repetitions and after correcting for measurement error. The diagonal terms represent successful detection rates with an average SP of 44.4(3)% after the first round, which increases to 49.6(3)% with the second iteration. The performance degradation of target states closer to $|00\rangle$ is caused by the less-efficient implementations of the corresponding oracles, where more single-qutrit rotations are required for the CPhase gate decomposition (see Appendix E). As promised by the algorithm, experimental detection probabilities for the individual correct states increased after the second iteration for all cases (except for $|02\rangle$ and $|12\rangle$, which we attribute to the lower lifetime of Q_2's $|2\rangle$ level). The experimental outcome also has a good agreement with our Master equation simulation as described in Appendix H indicating dephasing and cross-Kerr limited performance. The average experimental SPs beat the classical rates of 11.1% and 22.2% for the two rounds by more than a factor of 2, with clear improvement in performance after the second iteration.

IV. CONCLUSION

We demonstrate a fully programmable two-qutrit superconducting processor based on transmons. We utilize a linear coupler to obtain excellent connectivity in the underlying Hilbert space through parametrically activated fast entangling operations. The success probabilities of all the algorithms implemented, namely Deutsch-Jozsa, Bernstein-Vazirani, and Grover's search, are significantly higher than corresponding classical rates. Notably, we achieve improved success rates in finding the correct answer after performing the second iteration of Grover's search. To our knowledge, this is the *first experimental demonstration* of two-qutrit Grover's search across all quantum computing platforms. The performance of the processor is currently limited by low coherence times and cross-Kerr interaction, and we expect significant improvement with increased coherence [32, 33], pulse shaping [50], geometrical optimization [51, 52], and improved readout [30]. Our results indicate that qutrit-based processors could be a promising candidate for building a large-scale quantum computer and we believe, will foster investigations in the field of ternary quantum information processing.

ACKNOWLEDGMENTS

This work was supported by AFOSR Grant No. FA9550-19-1-0399 and ARO Grant No. W911NF-17-S-0001. Devices are fabricated in the Pritzker Nanofabrication Facility at the University of Chicago, which receives support from Soft and Hybrid Nanotechnology Experimental (SHyNE) Resource (NSF ECCS-1542205), a node of the National Science Foundation's National Nanotechnology Coordinated Infrastructure. This work also made

use of the shared facilities at the University of Chicago Materials Research Science and Engineering Center.

Appendix A: Single-qutrit gates

The native operations accessible for a single qutrit are

$$R_{01}(\phi,\theta)=\begin{bmatrix}\cos\frac{\theta}{2} & -e^{-i\phi}\sin(\theta/2) & 0\\ e^{i\phi}\sin\frac{\theta}{2} & \cos\frac{\theta}{2} & 0\\ 0 & 0 & 1\end{bmatrix}, \tag{A1a}$$

$$R_{12}(\phi,\theta)=\begin{bmatrix}1 & 0 & 0\\ 0 & \cos\frac{\theta}{2} & -e^{-i\phi}\sin(\theta/2)\\ 0 & e^{i\phi}\sin\frac{\theta}{2} & \cos\frac{\theta}{2}\end{bmatrix}, \tag{A1b}$$

$$\Theta(x,y)=\begin{bmatrix}1 & 0 & 0\\ 0 & e^{ix} & 0\\ 0 & 0 & e^{i(x+y)}\end{bmatrix}, \tag{A1c}$$

where, $R_{01}(\phi,\theta)$ and $R_{12}(\phi,\theta)$ are performed through sending drives at $|0\rangle \leftrightarrow |1\rangle$ and $|1\rangle \leftrightarrow |2\rangle$ transitions respectively with appropriate lengths and phases. However, the generic phase gate $\Theta(x,y)$ is implemented virtually as it requires no physical pulses. For each qutrit we record two phase parameters θ_{01} and θ_{12} corresponding to the pulses applied to the $|0\rangle \leftrightarrow |1\rangle$ and $|1\rangle \leftrightarrow |2\rangle$ transitions respectively. To apply the $\Theta(x,y)$ gate, we advance both θ_{01} and θ_{12} by x and y for all the subsequent pulses. The single-qutrit Z gate becomes a special case of the generic phase gate: $Z=\Theta\left(\frac{2\pi}{3},\frac{2\pi}{3}\right)$. Since, all phase updates are performed in software, the Z gate (or a $\Theta(x,y)$ gate) has nearly 100% fidelity.

An arbitrary single-qutrit unitary can be constructed using combinations of Eqs. (A1). For example, the H gate is deconstructed as

$$\begin{aligned}H&=\frac{1}{\sqrt{3}}\begin{bmatrix}1 & 1 & 1\\ 1 & e^{\frac{2\pi}{3}i} & e^{\frac{4\pi}{3}i}\\ 1 & e^{\frac{4\pi}{3}i} & e^{\frac{2\pi}{3}i}\end{bmatrix}\\ &=R_{12}\left(0,\frac{\pi}{2}\right)\cdot R_{01}(0,\beta)\cdot\Theta\left(\pi,\frac{\pi}{2}\right)\cdot R_{12}\left(0,\frac{\pi}{2}\right)\cdot\Theta(0,\pi),\end{aligned} \tag{A2}$$

with $\beta=2\tan^{-1}(\sqrt{2})$. Similarly, the bit-shift gate is decomposed as

$$X=\begin{bmatrix}0 & 0 & 1\\ 1 & 0 & 0\\ 0 & 1 & 0\end{bmatrix}=R_{01}(0,\pi)\cdot R_{12}(0,\pi). \tag{A3}$$

For single-qutrit process tomography, we use nine different initial states: $\{|j\rangle,\ (|j\rangle+|k\rangle)/\sqrt{2},\ (|j\rangle+i|k\rangle)/\sqrt{2}\},\ \{j,k\}\in\{0,1,2\}$. We obtain process fidelities of 98.96% (Q_1) and 97.06% (Q_2) for the H gate as shown in Fig. 4. The same for the Z gates are 97.48% (Q_1) and 96.76% (Q_2). Even though the Z gates should be nearly perfect, the process fidelities are limited by state preparation and measurement (SPAM) error. Further, it is expected that the process fidelity for the Z gate should be larger than that of the H gate, which requires multiple physical pulses. One explanation for the opposite experimental observation is as follows. First, the relaxation time of level $|2\rangle$ is smaller than that of level $|1\rangle$ whereas the detection probability of level $|0\rangle$ remains very large after a finite time when initialized at $|0\rangle$ (set by the thermal excitation). The action of H gate on the chosen nine initial states always results in some superposition state where all three basis components $|0\rangle, |1\rangle,$ and $|2\rangle$ participate. But for the case of Z-gate, several final states have a population in $|1\rangle$ and $|2\rangle$ or a superposition of those. As a result, the final states for the case of Z gate experience stronger relaxation error reducing the fidelity of the process tomography.

All single-qutrit gates use rectangular pulses with Gaussian edges. The envelope shape $h(t)$ is defined in Eq. (A4) with $\sigma=2.5$ ns,

$$h(t)=\begin{cases}A_0 e^{\frac{-(t-t_0-2\sigma)^2}{2\sigma^2}} & \text{if } t_0<t<t_0+2\sigma,\\ A_0 & \text{if } t_0+2\sigma<t<t_1-2\sigma,\\ A_0 e^{\frac{-(t_1-2\sigma-t)^2}{2\sigma^2}} & \text{if } t_1-2\sigma<t<t_1,\\ 0 & \text{Otherwise,}\end{cases} \tag{A4}$$

where, 2σ is the Gaussian tail length, A_0 is the amplitude, and t_1-t_0 is the total pulse length.

Appendix B: Device fabrication and parameters

The device was fabricated on a 430 μm thick C-plane sapphire substrate annealed at 1200°C for 2 hours. A 200 nm thick film of Tantalum was sputtered at 800^{o}C to form the ground plane. The large features (excluding the Josephson junctions) were made via optical lithography followed by wet-etching (dipped for 20 seconds) at wafer-scale using Transene Tantalum etchant 111. A 600 nm thick layer of AZ 1518 was used as the (positive) photoresist, and a Heidelberg MLA 150 Direct Writer (405 nm laser) was used for the photolithography. The photoresist was developed by dipping in to MIF 300 developer for 1 minute and removed by immersing inside 80°C NMP for four hours after wet-etching. The junction mask was fabricated via electron-beam lithography

Gate type	On Q_1 (ns)	On Q_2 (ns)
$\pi/2_{01}$	49.50	49.71
$\pi/2_{12}$	41.27	44.15
π_{01}	94.98	95.41
π_{12}	78.52	84.28
Z	0	0
H	141.88	147.90

TABLE I. Total gate lengths for different single-qutrit operations. The Z gates are implemented virtually.

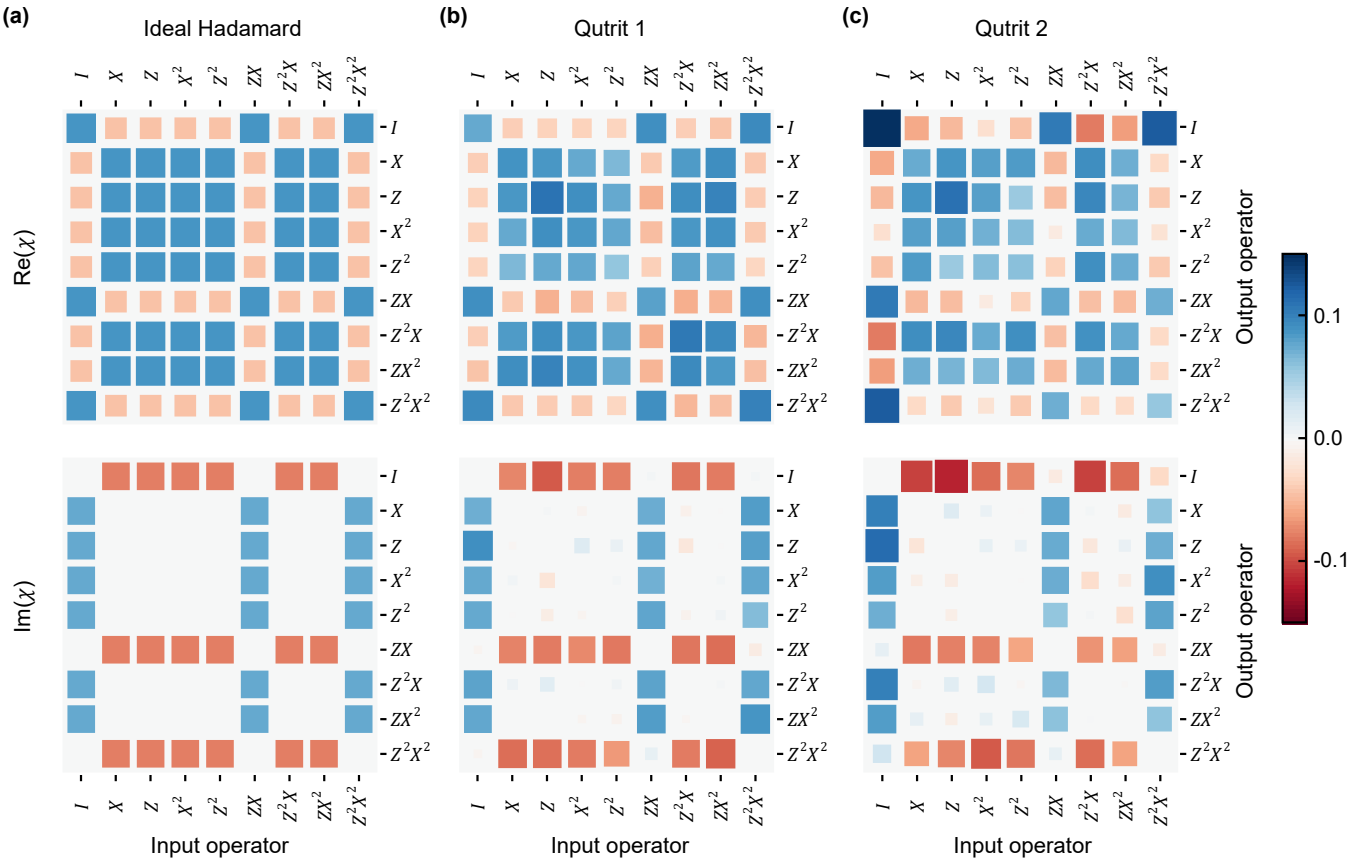

FIG. 4. Process tomography for Hadamard gates. The top and bottom panels show real and imaginary components of the process matrix (χ) for (a) an ideal case, (b) Q_1, and (c) Q_2.

using a Raith EBPG5000 Plus E-Beam Writer on a bi-layer resist (MMA-PMMA) comprising of MMA EL11 and 950PMMA A7. Both small (transmon) and large (coupler) Josephson junctions were made with the Dolan bridge technique. Those were subsequently evaporated in a Plassys electron-beam evaporator with double angle evaporation ($\pm 23^o$). The wafer was then diced into 7×7 mm chips, lifted-off, mounted on a printed circuit board, and subsequently wire-bonded. The coherence times and frequency parameters are listed in Table. II and Table. III.

Qutrit	$T_1^{01}(\mu s)$	$T_1^{12}(\mu s)$	$T_{2R}^{01}(\mu s)$	$T_{2R}^{12}(\mu s)$
Q_1	47.9	21.7	4.5	2.0
Q_2	35.1	3.9	3.2	2.4

TABLE II. Device coherence parameters. T_1^{jk} and T_{2R}^{jk} respectively represent the relaxation and Ramsey dephasing time constants for the $|j\rangle \leftrightarrow |k\rangle$ transition.

Appendix C: Hamiltonian

We develop a simplified model to extract various parameters and explain the sideband interactions. Omitting the readout resonators, the bare Hamiltonian can be expressed as

$$H_0 = \vec{q}^{\intercal} C_L^{-1} \vec{q} - E_{J1}\cos(\phi_c - \phi_1) - E_{J2}\cos(\phi_c - \phi_2), \\ - E_{Jc}\cos\left(2\pi\frac{\Phi_{\text{ext}}}{\Phi_0}\right)\cos(\phi_c), \tag{C1}$$

with the capacitance matrix

$$C_L = \begin{bmatrix} C_1 + C_{12} & -C_{12} & 0 \\ -C_{12} & C_2 + C_{12} & 0 \\ 0 & 0 & C_1 + C_2 + C_c \end{bmatrix}. \tag{C2}$$

Here $\{\phi_1, \phi_2, \phi_c\}$ are the node fluxes for the two qubits and the coupler respectively. $\vec{q}^{\intercal} = (q_1, q_2, q_c)$ represent the charge vector conjugate to the node fluxes, so that $[\phi_k, q_k] = i$. The coupler capacitance C_c originates from the self-capacitance of the large coupler junctions.

Parameter	Symbol	Value/2π
Q_1 $\|0\rangle \leftrightarrow \|1\rangle$ transition	ω_1	3.3494 (GHz)
Q_2 $\|0\rangle \leftrightarrow \|1\rangle$ transition	ω_2	3.8310 (GHz)
Q_1 anharmonicity	α_1	-115.2 (MHz)
Q_2 anharmonicity	α_2	-159.8 (MHz)
Readout1 frequency	ω_{r1}	4.9602 (GHz)
Readout2 frequency	ω_{r2}	5.4225 (GHz)
$(E_{\|11\rangle} - E_{\|01\rangle}) - (E_{\|10\rangle} - E_{\|00\rangle})$	ZZ	-238 (kHz)
$(E_{\|21\rangle} - E_{\|11\rangle}) - (E_{\|20\rangle} - E_{\|10\rangle})$	ZZ_{2110}	-148 (kHz)
$(E_{\|12\rangle} - E_{\|11\rangle}) - (E_{\|02\rangle} - E_{\|01\rangle})$	ZZ_{1021}	-183 (kHz)
$(E_{\|22\rangle} - E_{\|12\rangle}) - (E_{\|20\rangle} - E_{\|10\rangle})$	ZZ_{2120}	-211 (kHz)
$(E_{\|22\rangle} - E_{\|21\rangle}) - (E_{\|02\rangle} - E_{\|01\rangle})$	ZZ_{2021}	-262 (kHz)
$(E_{\|12\rangle} - E_{\|02\rangle}) - (E_{\|10\rangle} - E_{\|00\rangle})$	ZZ_{1020}	-402 (kHz)
$(E_{\|21\rangle} - E_{\|20\rangle}) - (E_{\|01\rangle} - E_{\|00\rangle})$	ZZ_{2010}	-403 (kHz)
Coefficient of $(a^\dagger a)(b^\dagger b)$	J_{11}	-304.3 (kHz)
Coefficient of $(a^\dagger a)^2(b^\dagger b)$	J_{21}	37.8 (kHz)
Coefficient of $(a^\dagger a)(b^\dagger b)^2$	J_{12}	23.6 (kHz)
Coefficient of $(a^\dagger a)^2(b^\dagger b)^2$	J_{22}	5.4 (kHz)

TABLE III. Experimentally obtained various frequency parameters.

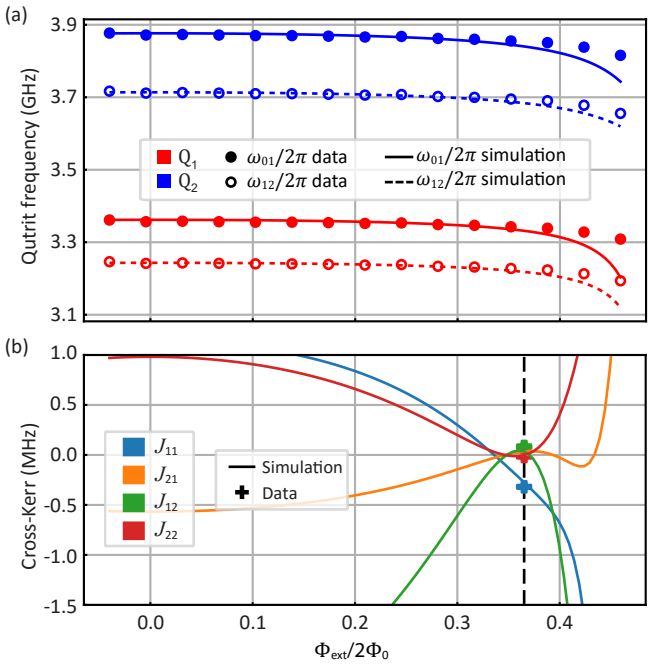

FIG. 5. Circuit quantization results. (a) Comparison of the experimentally obtained $|0\rangle \leftrightarrow |1\rangle$ transition frequency ω_{01} (solid circle) and $|1\rangle \leftrightarrow |2\rangle$ transition frequency ω_{12} (hollow circle) as a function of Φ_{ext} with simulations (solid/dashed lines) for qutrits Q_1 (red) and Q_2 (blue). (b) Different cross-Kerr parameters J_{11} (magenta), J_{21} (orange), J_{12} (green), J_{22} (brown) as a function of Φ_{ext}. The solid lines are obtained from the numerical calculation, and the experimental values at the operating flux-bias (dashed line) are shown with plus symbols.

We first extract the linear part of the Hamiltonian,

$$H_{\text{lin}} = \vec{q}^{\,\intercal} C_L^{-1} \vec{q} + \frac{E_{J1}}{2}(\phi_c - \phi_1)^2 + \frac{E_{J2}}{2}(\phi_c - \phi_2)^2 + \frac{E_{Jc}}{2}\cos\left(2\pi\frac{\Phi_{\text{ext}}}{\Phi_0}\right)\phi_c^2. \quad \text{(C3)}$$

Table. IV includes all coefficients used in the simulation. We rewrite the charge and phase variables in the dressed basis such that H_{lin} is simultaneously diagonalized for both $\vec{n}$ and $\vec{\phi}$ with the transformation matrix U:

$$H_{\text{lin}} = \sum_{k=1,2,c}\left(\tilde{C}_k\tilde{n}_k^2 + \tilde{D}_k\tilde{\phi}_k^2\right) \quad \text{(C4a)}$$

$$\vec{\tilde{n}} = (\tilde{n}_1, \tilde{n}_2, \tilde{n}_c)^{\intercal} = U^{-1}\vec{n} \quad \text{(C4b)}$$

$$\vec{\tilde{\phi}} = \left(\tilde{\phi}_1, \tilde{\phi}_2, \tilde{\phi}_c\right)^{\intercal} = U^{-1}\vec{\phi} \quad \text{(C4c)}$$

$$U = \begin{bmatrix} U_{11} & U_{12} & U_{1c} \\ U_{21} & U_{22} & U_{2c} \\ U_{c1} & U_{c2} & U_{cc} \end{bmatrix}. \quad \text{(C4d)}$$

Then we quantize the circuit on the dressed basis,

$$\tilde{n}_k = \frac{i}{\sqrt{2}}\sqrt{\frac{\tilde{D}_k}{\tilde{C}_k}}\left(a_k^\dagger - a_k\right), \quad \text{(C5a)}$$

$$\tilde{\phi}_k = \frac{1}{\sqrt{2}}\sqrt{\frac{\tilde{C}_k}{\tilde{D}_k}}\left(a_k^\dagger + a_k\right), \quad \text{(C5b)}$$

Capacitance	(fF)	Josephson energy	(GHz)
C_{q1}	178.0	E_{J1}	13.6
C_{q2}	131.0	E_{J2}	13.3
C_c	193.6	E_{Jc}	1140.0
C_{q12}	2.0		

TABLE IV. Estimated capacitances and Josephson energies. Capacitances are extracted from Ansys Q3D simulations. Josephson energies are estimated using Ambegaokar-Baratoff relation and room temperature resistances of on-chip (nominally identical) test junctions.

and insert the nonlinear part back into the Hamiltonian,

$$\begin{aligned} H_{\rm tot} = & \sum_{k=1,2,c} \left(\tilde{C}_k \tilde{n_k}^2\right) \\ & - E_{J1} \cos\left(\sum_{k=1,2,c} \left(U_{ck}\tilde{\phi}_k - U_{1k}\tilde{\phi}_k\right)\right) \\ & - E_{J2} \cos\left(\sum_{k=1,2,c} \left(U_{2k}\tilde{\phi}_k - U_{ck}\tilde{\phi}_k\right)\right) \\ & - E_{Jc} \cos\left(2\pi\frac{\Phi_{\rm ext}}{\Phi_0}\right) \cos\left(\sum_{k=1,2,c} U_{ck}\tilde{\phi}_k\right). \end{aligned} \tag{C6}$$

The resulting transition frequencies and various ZZ interactions strengths as a function of $\Phi_{\rm ext}$ obtained from the numerical diagonalization along with the experimental data are shown in Fig. 5(a). We notice some deviation when the DC flux is biased very close to $\frac{\pi}{2}$. This is caused by the parasitic SQUID-loop inductance. However, around the DC flux position ($\Phi_{\rm ext}$ =0.185Φ_0) where we implement all quantum algorithms (vertical dashed line in Fig. 5(b)), we have a good match between the numerical and experimental data.

To understand how two-qutrit sidebands work, we follow Ref. [36] and apply adiabatic approximation to the Hamiltonian. The frequency of the coupler mode remains well above ($>$ 15 GHz) any other frequencies ($<$ 4 GHz) in the system and thus can be assumed to stay in the ground state during any operation. The static energy of the coupler mode is removed by minimizing the full circuit Hamiltonian. Treating qutrits as Duffing-type oscillators, a toy model with adiabatic approximation can be written as:

$$\begin{aligned} H_{\rm toy} =& \omega_1 a_1^\dagger a_1 + \omega_2 a_2^\dagger a_2 + \frac{\alpha_1}{2} a_1^\dagger a_1^\dagger a_1 a_1 + \frac{\alpha_2}{2} a_2^\dagger a_2^\dagger a_2 a_2 \\ & + g_1(t)\left(a_1^\dagger + a_1\right)\left(a_2^\dagger + a_2\right) \\ & + g_2\left(-a_1^\dagger + a_1\right)\left(-a_2^\dagger + a_2\right), \end{aligned} \tag{C7a}$$

$$g_1(t) = \frac{\sqrt{E_{J1}E_{J2}}}{2E_{Jc}\cos\left(2\pi\Phi_{\rm ext}(t)/\Phi_0\right)}\sqrt{\omega_1\omega_2}, \tag{C7b}$$

$$g_2 = \frac{\sqrt{C_1C_2}}{2C_{12}}\sqrt{\omega_1\omega_2}. \tag{C7c}$$

Here $g_1(t)$ and g_2 are inductive and capacitive coupling strengths respectively. $g_1(t)$ is flux tunable, and when the RF flux modulation frequency matches with any two-photon transition frequency $|jk\rangle \leftrightarrow |j+1, k-1\rangle$ or $|jk\rangle \leftrightarrow |j+1, k+1\rangle$, the corresponding sideband is activated in the system. This adiabatic approximation requires sideband frequencies to be much smaller than qutrit frequencies, which can capture the (red) sideband rates for $|22\rangle \leftrightarrow |31\rangle$ and $|21\rangle \leftrightarrow |30\rangle$ used in the system. However, the (blue) sideband rate for $|jk\rangle \leftrightarrow |j+1, k+1\rangle$ cannot be explained with such an approximation and requires keeping the coupler mode in the analysis [53].

Appendix D: Sideband calibrations

We utilize sideband interactions to implement various entangling operations in the two-qutrit subspace. The tune-up of these gates are very easy and are similar to single-qubit Rabi experiments. We use a Gaussian-flatten pulse shape for all flux modulation drives, with 5 ns ramping and descending time. We initialize the qutrits in relevant states and sweep both frequency and the flat length of the flux modulation drive $\Phi_{\rm ext}(t)$ to obtain a Chevron pattern. We demonstrate Chevron patterns for the six red sidebands in Fig. 6 and for the four blue sidebands in Fig. 7 at separately optimized pump amplitudes. The plots show average photon numbers on the qutrits as a function of time and drive frequencies. The resonance feature is selected at the drive frequency where the oscillation shows maximum contrast, as represented by the red dashed lines. We plot the line cuts along these selected frequencies for all the ten sidebands in Fig. 8 and use the traces to extract interaction rates and gate times.

The red sidebands that coherently take the population out of the computational subspace, namely $|21\rangle \leftrightarrow |30\rangle$ and $|22\rangle \leftrightarrow |31\rangle$ are utilized to implement elementary CPhase gates as discussed in the next section. Other four red sidebands within the computational space can be utilized to implement iSWAP gates between relevant levels. The four blue sidebands generate or extract two photons simultaneously and can be utilized to generate various entangled states. For example, two sequential pulses at $|00\rangle \leftrightarrow |11\rangle$ and $|11\rangle \leftrightarrow |22\rangle$ with appropriate lengths and phases can generate the two-qutrit EPR state $(|00\rangle + |11\rangle + |22\rangle)/\sqrt{3}$.

We have not used the blue sidebands for the algorithms

Sideband	Type	Rate (MHz)	π length (ns)
$\|10\rangle \leftrightarrow \|01\rangle$	Red	20.1	30.2
$\|20\rangle \leftrightarrow \|11\rangle$	Red	21.2	27.5
$\|02\rangle \leftrightarrow \|11\rangle$	Red	20.3	29.7
$\|21\rangle \leftrightarrow \|12\rangle$	Red	35.8	17.5
$\|21\rangle \leftrightarrow \|30\rangle$	Red	19.3	29.9
$\|22\rangle \leftrightarrow \|31\rangle$	Red	11.2	50.2
$\|00\rangle \leftrightarrow \|11\rangle$	Blue	3.9	158.5
$\|10\rangle \leftrightarrow \|21\rangle$	Blue	3.5	142.6
$\|01\rangle \leftrightarrow \|12\rangle$	Blue	4.6	115.0
$\|11\rangle \leftrightarrow \|22\rangle$	Blue	8.4	66.6

TABLE V. Sideband rates and gate lengths for various interactions achieved with the device. The π-pulse lengths include both the flat-top part and 5 ns rising and falling Gaussian tail of the pulse. The distortion observed for the $|01\rangle \leftrightarrow |12\rangle$ Chevron is most likely due to the stray charge coupling of the flux line to the SQUID loop (see text for details).

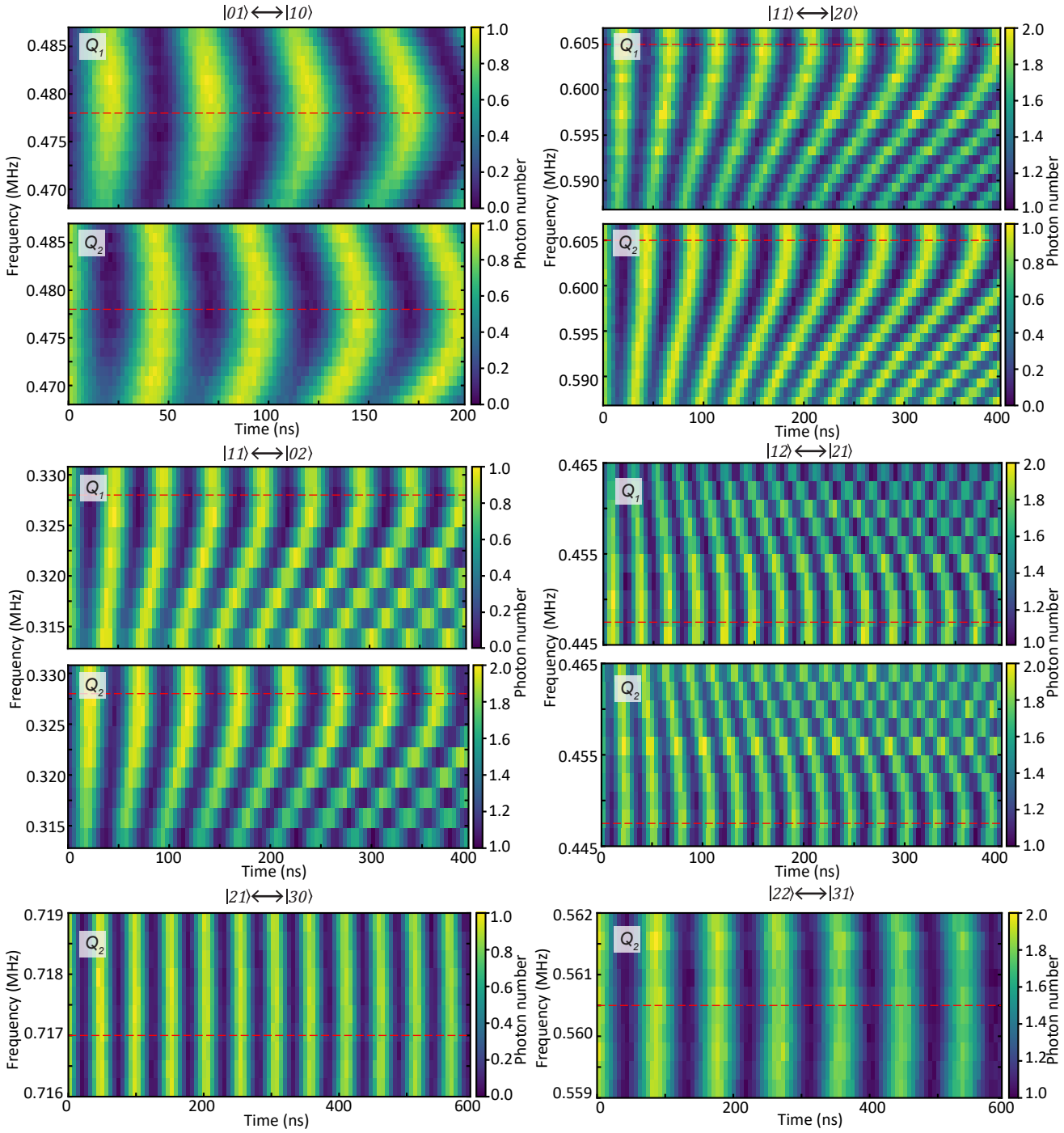

FIG. 6. Chevron plots for the six two-qutrit red sidebands. All sidebands are parametrically activated by modulating the coupler at the corresponding transition frequencies. Pulses used for flux modulations have a rectangular shape with 5 ns long rising and falling Gaussian-shaped edges. The x-axis represents the length of the flat-top section. Both qutrits are simultaneously read out, and each data point is an average of 1000 experiments.
* Q_1's readout are not shown in the $|21\rangle \leftrightarrow |30\rangle$ and $|22\rangle \leftrightarrow |31\rangle$ cases, as the readout on $|3\rangle$ is not optimized.

due to lower rates. While theoretically larger rates should be achievable, we start to observe readout saturation [51] and distortions in the Chevron plots as visible in case of $|01\rangle \leftrightarrow |12\rangle$ sideband (see Fig. 7). This distortion is most likely caused by the flux line's stray charge coupling to the coupler SQUID. The unwanted charge coupling, particularly at high (blue sideband) frequencies, result in asymmetrical parametric modulation [51, 52] of the SQUID loop. This effect can be solved by optimizing flux line geometry, allowing stronger blue sideband rates.

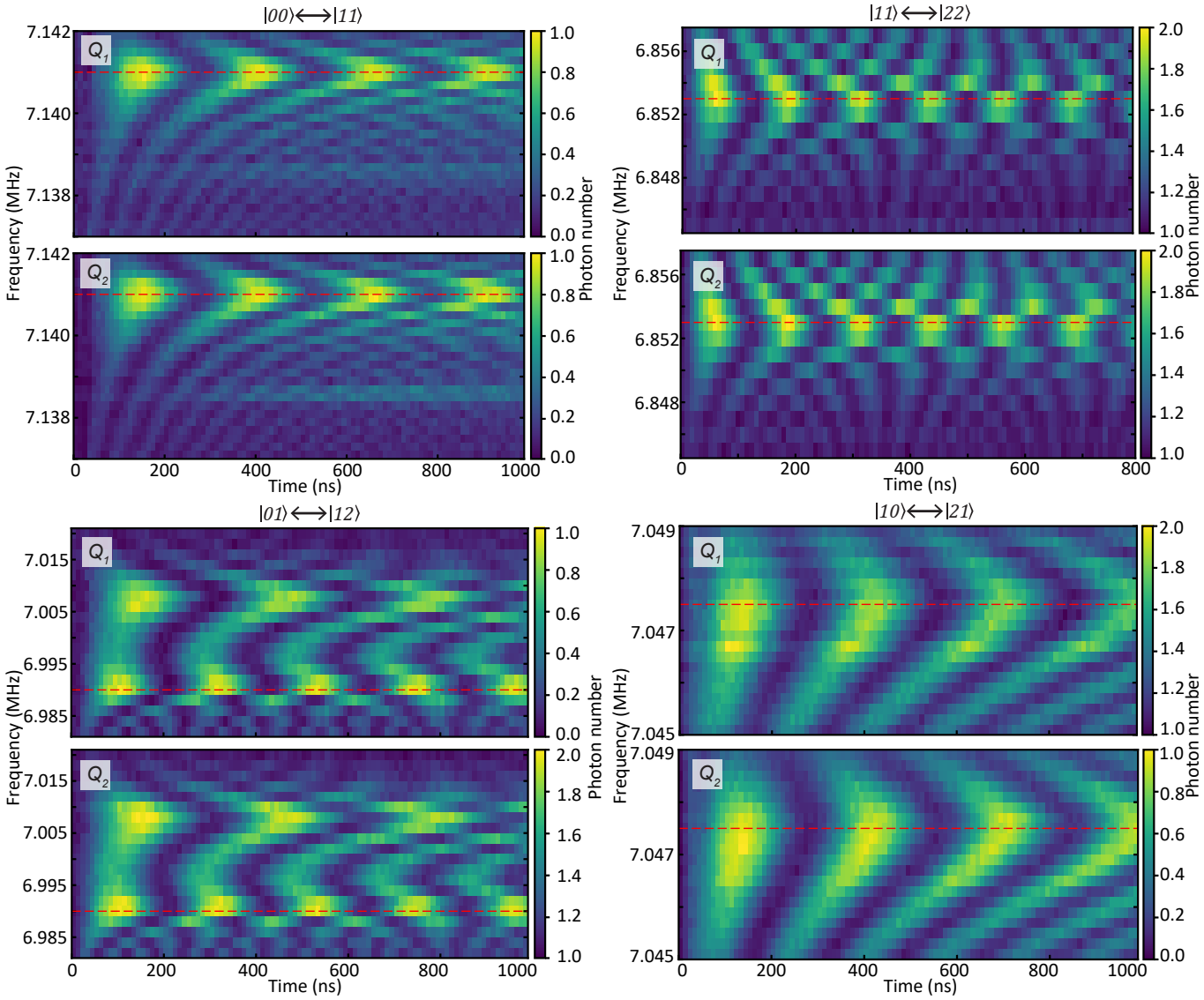

FIG. 7. Chevron plots for the four two-qutrit blue sidebands. Sidebands are all parametrically activated through flux modulation of the coupler at relevant frequencies. Pulses used for flux modulations have a rectangular shape with 5 ns long rising and falling Gaussian-shaped edges, and the x-axis represents the length of the flat-top section. Each experimental data is an average of 1000 measurements.

Appendix E: CPhase gates

As shown in Fig. 9(a), we utilize two native CPhase gates $C_\theta\left(\theta, |21\rangle\right)$ and $C_\theta\left(\theta, |22\rangle\right)$, which can be realized by applying two π rotations to $|21\rangle \leftrightarrow |30\rangle$ and $|22\rangle \leftrightarrow |31\rangle$ transitions with the phase of the second π pulse being advanced by $\pi - \theta$ compared to the the first one. The optimized gate lengths are 55.9 ns and 94.0 ns for $C_\theta\left(\theta, |21\rangle\right)$ and $C_\theta\left(\theta, |22\rangle\right)$ respectively.

The CPhase gates on the states in the region (2), (4) and (6) (highlighted with yellow) need to decomposed where the number indicates the number single-qutrit rotations required. The decomposition starts from the target state, followed by the application of single-qutrit rotations to arrive at one of the states in the region (0) (following brown arrows). After applying the native CPhase gate, reverse single-qutrit rotations are administered traversing the same path back to the target state. Fig. 9(b) shows the circuit decomposition of $C_\theta\left(\pi, |00\rangle\right)$ as an example, which requires the maximum number of pulses. One can also use combinations of red and blue sidebands to further reduce the total number of gates. Note that, even though we have access to $C_\theta\left(\pi, |12\rangle\right)$, we do not use it due to poorer fidelity caused by significantly lower lifetime of the $|2\rangle$ and $|3\rangle$ levels of Q_2.

The calibration of the CPhase gates involves compensation for the additional phases acquired during the gate operation [54]. In our coupler, both the AC stark shift and the rectification effect from SQUID flux modulation can cause qutrit frequencies to change during the gate, re-

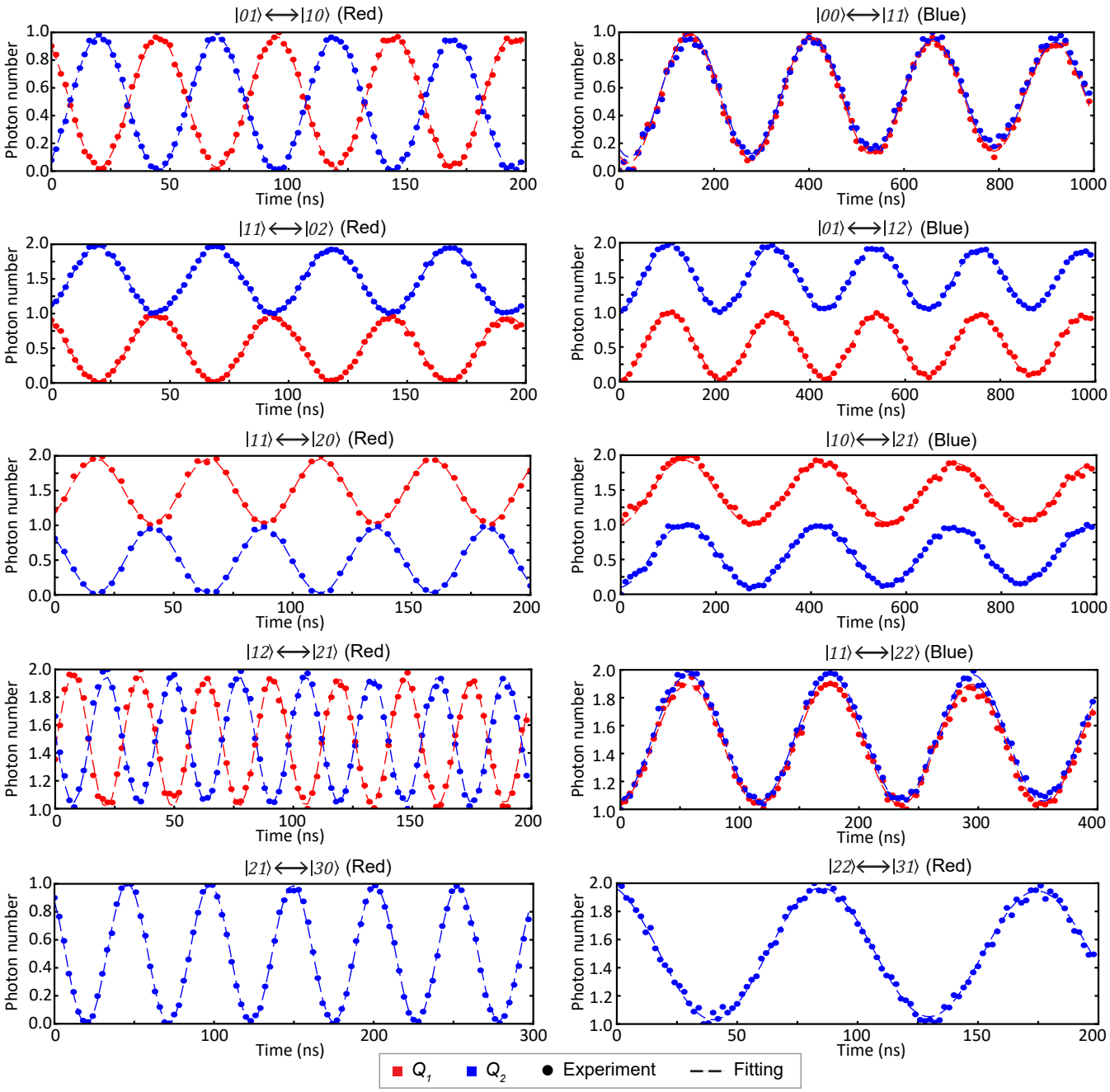

FIG. 8. Coherent oscillations for all two-qutrit sidebands. On-resonance features from the Chevron plots are selected and fitted to extract the sideband rates and π rotation lengths (shown in Table. V). Rectangular pulses with 5 ns long Gaussian edges are used for flux modulations, and the x-axis represents the length of the flat-top section. Each data point is an average of 1000 experiments.

sulting in extra phases $\beta_{01}^{(j)}$ and $\beta_{12}^{(j)}$ for the $|0\rangle \leftrightarrow |1\rangle$ and $|1\rangle \leftrightarrow |2\rangle$ transitions of the j-th qutrit. We use the circuit shown in Fig. 9(c) to extract these additional phases. Starting from the ground state, we apply the gate $G_1 = R_{01}\left(0, \frac{\pi}{2}\right)$ to both qutrits if calibrating $\beta_{01}^{(j)}$, followed by $C_\theta\left(0, |jk\rangle\right)$ and sweep the virtual phase $Z_\theta = \Theta(\theta, 0)$ before the last gate $G_2 = R_{01}\left(\pi, \frac{\pi}{2}\right)$ on Q_j. By fitting the readout on Q_j to $C_0 + C_1 \sin\left(\beta_{01}^{(j)} + \theta\right)$, one can extract the extra phase $\beta_{01}^{(j)}$ acquired. A similar procedure is used to extract $\beta_{12}^{(j)}$ where we use $G_1 = R_{12}\left(0, \frac{\pi}{2}\right) \cdot R_{01}\left(0, \pi\right)$, $G_2 = R_{12}\left(\pi, \frac{\pi}{2}\right)$, and $Z_\theta = \Theta(0, \theta)$. Hence, each CPhase gate has four virtual phases corresponding to two native transitions for each qutrit. As a demonstration, we apply the CPhase gate $C_\theta\left(\frac{8\pi}{9}, |22\rangle\right)$ on the state

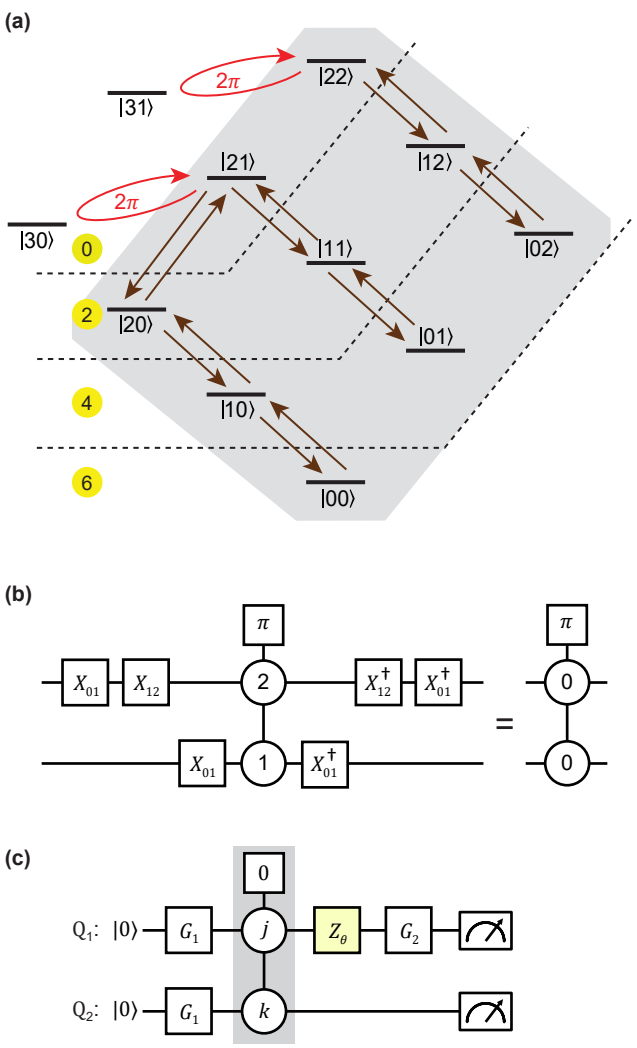

FIG. 9. CPhase gate construction. (a) Partitioned energy level diagram. Flipping the phase of a specific target state in region (0) is performed through a 2π sideband rotation (shown in red arrow). Flipping the other target states requires a decomposition. The application of a $C_\theta(\pi, |mn\rangle)$ follows the path marked with brown arrows starting from $|mn\rangle$. Here the numbers inside the yellow circle indicate the total number of single-qutrit π pulses required. (b) An example of circuit decomposition for the $C_\theta(\pi, |00\rangle)$ gate. (c) Single-qutrit phase compensation calibration for a $C_\theta(\pi, |jk\rangle)$ gate.

$\frac{1}{3}(|0\rangle + |1\rangle + |2\rangle)^{\otimes 2}$ (with initial state fidelity of 87.7%). The final state (shown in Fig. 10) obtained after two-qutrit tomography [55] shows a fidelity of 82.4%, which is limited by the cross-Kerr coupling between qutrits and SPAM error.

Appendix F: Measurement error mitigation

Figure 11 shows the single-shot assignment probability for the nine basis states of our two-qutrit processor. We refer this 2d array as the confusion matrix. Our readout

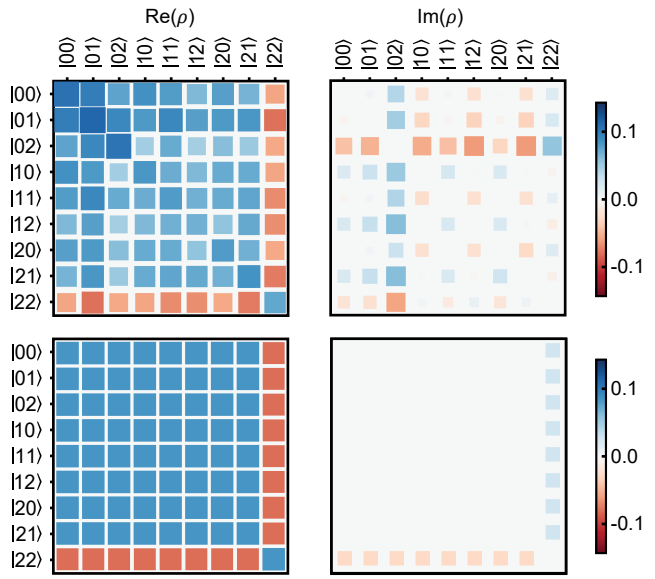

FIG. 10. Two-qutrit tomography of the state $\frac{1}{3}(|0\rangle + |1\rangle + |2\rangle)^{\otimes 2}$ after applying the CPhase gate $C_\theta\left(\frac{8\pi}{9}, |22\rangle\right)$. The top and bottom rows are experimental and ideal density matrices, with the real and imaginary parts shown in the left and right columns.

fidelity is limited because there are no parametric amplifiers on the output lines. To fairly demonstrate the performance of the qutrit algorithms with single shot results, we apply the inverse of the confusion matrix to the readout results to compensate for the measurement error. After correcting for the measurement error, it is possible that some of the readout counts (number of times the system found in a specific state) become negative, which happens due to drifts in the calibration parameters.

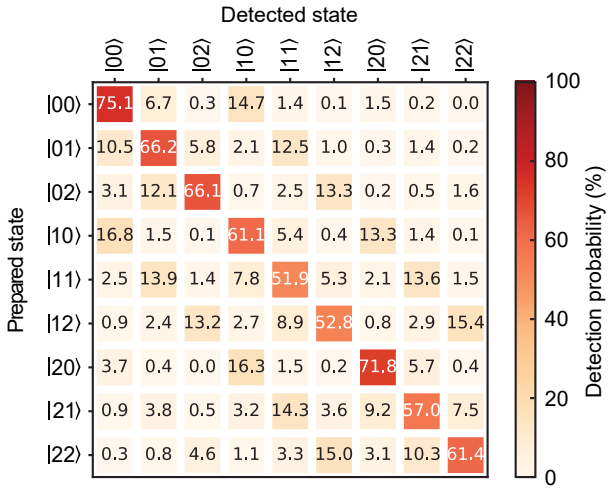

FIG. 11. Heatmap of the confusion matrix. 3^2 basis states are prepared and measured for 20,000 times. The numbers represent average assignment probabilities.

This is corrected using Maximum-Likelihood-Estimation (MLE) with the assumption that the minimum fluctuation of a measurement repeated N times should not be lower than $\sqrt{N}$ (assuming normal distribution). We define the following cost function to avoid non-physical measurement counts:

$$f_c(\overrightarrow{p}, \overrightarrow{q}) = \sum_{j=1}^{9} \left(\frac{p_j - q_j}{q_j} \right)^2, \tag{F1}$$

with the restriction $p_j \geq \sqrt{N}$. Here $\overrightarrow{q}$ contains the experiment counts (1d array of 9 elements corresponding to the basis states) after applying the inverse of the confusion matrix, and $\overrightarrow{p}$ is the extracted counts after MLE.

Appendix G: Balanced oracles of DJ algorithm

We implement 16 different balanced functions whose equivalent classical functions are tabulated in Table VI. We use A and B to represent the classical ternary values (0,1, and 2) for the two qutrits. The operator $\oplus$ and $\odot$ correspond to addition and multiplication modulo 3 respectively.

Oracle	Classical function	Oracle	Classical function
$Z \otimes I$	A $\oplus$ 0	$I \otimes Z$	0 $\oplus$ B
$Z \otimes X$	A $\oplus$ 1	$X \otimes Z$	1 $\oplus$ B
$Z \otimes X^2$	A $\oplus$ 2	$X^2 \otimes Z$	2 $\oplus$ B
$Z^2 \otimes I$	(2 $\odot$ A) $\oplus$ 0	$I \otimes Z^2$	0 $\oplus$ (2 $\odot$ B)
$Z^2 \otimes X$	(2 $\odot$ A) $\oplus$ 1	$X \otimes Z^2$	1 $\oplus$ (2 $\odot$ B)
$Z^2 \otimes X^2$	(2 $\odot$ A) $\oplus$ 2	$X^2 \otimes Z^2$	2 $\oplus$ (2 $\odot$ B)
$Z \otimes Z$	A $\oplus$ B	$Z \otimes Z^2$	A $\oplus$ (2 $\odot$ B)
$Z^2 \otimes Z$	(2 $\odot$ A) $\oplus$ B	$Z^2 \otimes Z^2$	(2 $\odot$ A) $\oplus$ (2 $\odot$ B)

TABLE VI. Equivalent classical functions (ternary valued) for the 16 balanced functions implemented in the Deutsch-Jozsa algorithm.

Appendix H: Error analysis

Multiple error sources limit us from approaching the theoretical success rates for different quantum algorithms. In order to extract contributions from different sources, we perform master equation simulations in the lab frame for Grover's search using the coherence and cross-Kerr parameters obtained experimentally. We consider a 4×4 dimensional Hilbert space describing the lowest four energy eigenstates of each transmon and insert three different error channels, namely, relaxation, dephasing, and static ZZ progressively. We do not include the inductive coupler in the simulation as it has a much higher resonance frequency (> 15 GHz) during any operation and thus should not be excited. We compute the squared statistical overlap (SSO) [42] between two sets of probability distribution $\vec{p}$ and $\vec{p'}$ defined as $\left(\sum_{j=0}^{8} \sqrt{p_j p'_j}\right)^2$ for each of the oracle implementation and then determine the mean value from nine different oracle applications. We first verify that in the absence of any error channel, our simulation produces probability distributions that are nearly identical with the ideal values. Next, we include the three error channels one by one and recompute the SSOs with respect to the ideal probability distribution with increased circuit depths. We tabulate the drop in SSOs after one and two rounds of Grover's search in Table. VII, which indicate their individual error contributions to the algorithm.

Two biggest error sources are the inter-qutrit dispersive coupling and the dephasing. The inter-qutrit dispersive coupling includes both the static-ZZ values measured in Table. III and the dynamic-ZZ terms induced during (parametric) gate operations. The ZZ interactions introduce unwanted phase accumulations that reduce the performance of both single-qutrit and CPhase gates. The dephasing noise is also a significant source of error. The deepest circuit (2 stages of Grover's search) implemented includes 17 single-qutrit and 4 two-qutrit gates, with a total execution time of 2.11 μs. This time becomes comparable to the qutrit's Ramsey times (see Table II) and strongly degrades the success rates. The third one is the relaxation time, and its contribution is smaller than the dephasing error as our qutrits' T_1 are typically longer than T_2. The fourth source is the leakage to non-computational levels. However, we use Gaussian-filtered rectangular pulses with maximum single-qutrit rotations rates being much smaller than the energy gaps, and thus errors due to leakage should not be significant. While we have not explicitly measured the leakage to the participating levels for the CPhase gates, from the continued contrast of the calibration curves (bottom two plots in Fig. 8), we anticipate a negligible effect. Besides, in our simulation, we keep the first 4 levels for the transmon to always include the leakage error. In order to verify that we have captured all the main sources of error, we compare the experimental results with simulated outcomes as shown in Fig. 12. Those show a very good agreement with SSOs of 94.0% and 97.1% for one and two stages of amplitude amplification.

Error channel	After 1 round	After 2 rounds
Relaxation (T_1)	0.83%	11.89%
Dephasing (T_ϕ)	2.70%	16.07%
Static ZZ	5.08%	13.38%

TABLE VII. Error budget for the two-qutrit Grover's search algorithm. Drops in SSOs after one and two rounds of amplitude amplification are shown due to different error channels.

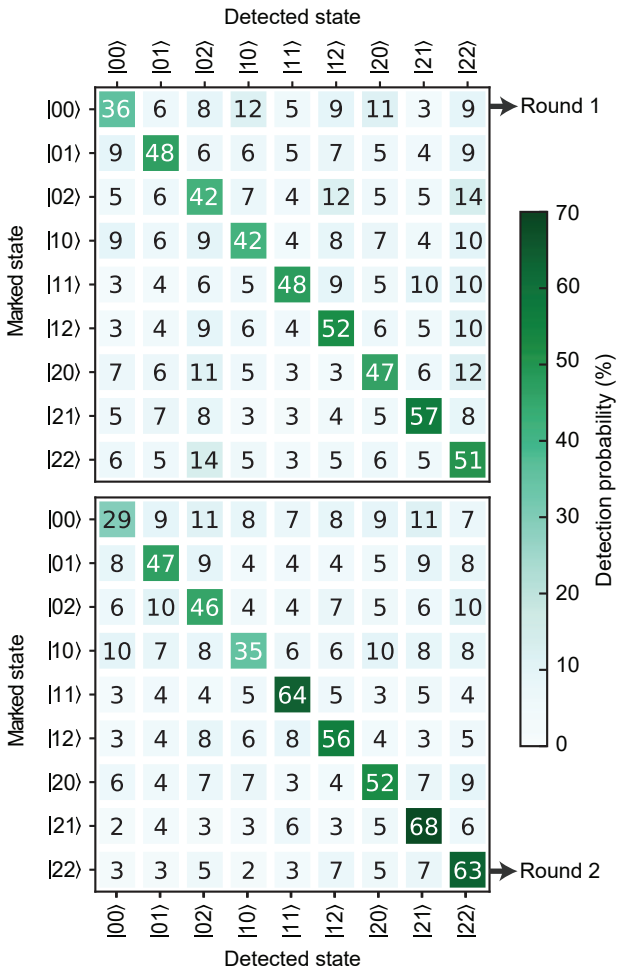

FIG. 12. Master equation simulation of two-qutrit Grover's search with one and two stages of amplitude amplification using experimentally measured parameters. These results are in good agreement with the experimental outcomes shown in Fig. 3(b) in the main text.

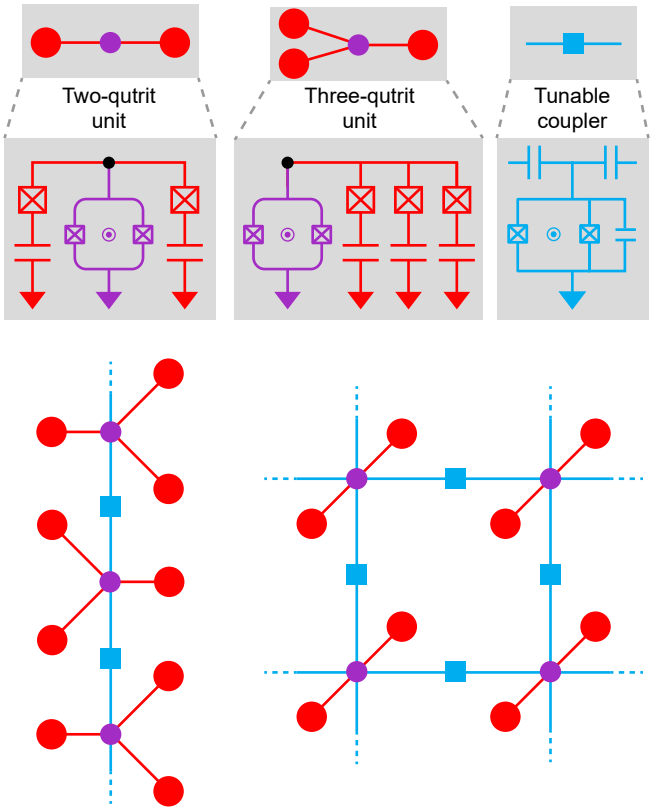

FIG. 13. Scaling-up schemes using qutrit-based units as building blocks.

Appendix I: Scaling up

We envisage building a larger system using qutrit-based units, and there are several choices. First, one can couple three transmons to the same parametric coupler [37] to build a three-qutrit processor where inter-qutrit static ZZ can be simultaneously minimized through an optimized layout ensuring almost identical inter-transmon capacitances. Next, these units can be used as building blocks to expand in a linear or planar geometry, as shown in Fig. 13. Two units could be coupled via commonly used tunable couplers [56–58] where a galvanic connection is not required. Any two qutrits between two neighboring units can be made equally distant (with respect to hopping) when the capacitive coupling for the inter-unit coupler is made to the central superconducting islands. This way one can realize a moderately-sized qutrit processor consisting of highly efficient two or three qutrit units with fast gates and a slightly slower but switchable interaction between neighboring pairs with almost identical rates.

Appendix J: Setup

The room and cryogenic temperature wiring diagram is illustrated in Fig 14. The device is placed inside a bilayer μ-metal shield, mounted on the base plate of a dilution fridge with 15 mK base temperature. A Tektronix 5014C (1.2 GSa/s) Arbitrary Waveform Generator (AWG) acts as the master trigger for all other equipment. The readout pulses are generated through two CW tones from RF sources (PSG-E8257D), modulated by the AWG 5014C. The qutrit pulses are generated through another 4-channel AWG (Keysight M8195 65 GSa/s, 16 GSa/s per channel). Before entering the fridge, the qutrit and readout pulses are combined and sent through lines In_1 and In_2. One DC source (Yokogawa GS200) is used to bias the coupler's DC flux position. The RF flux modulation is synthesized through the same 4-channel AWG. Two other direct charge drives, also synthesized through the same AWG, are not used in this project. Inside the fridge, at the 4K plate all input lines have 20 dB attenuation. At the base plate, In_1 and In_2 lines have 10-dB attenuation each, followed by a strong Eccosorb® provid-

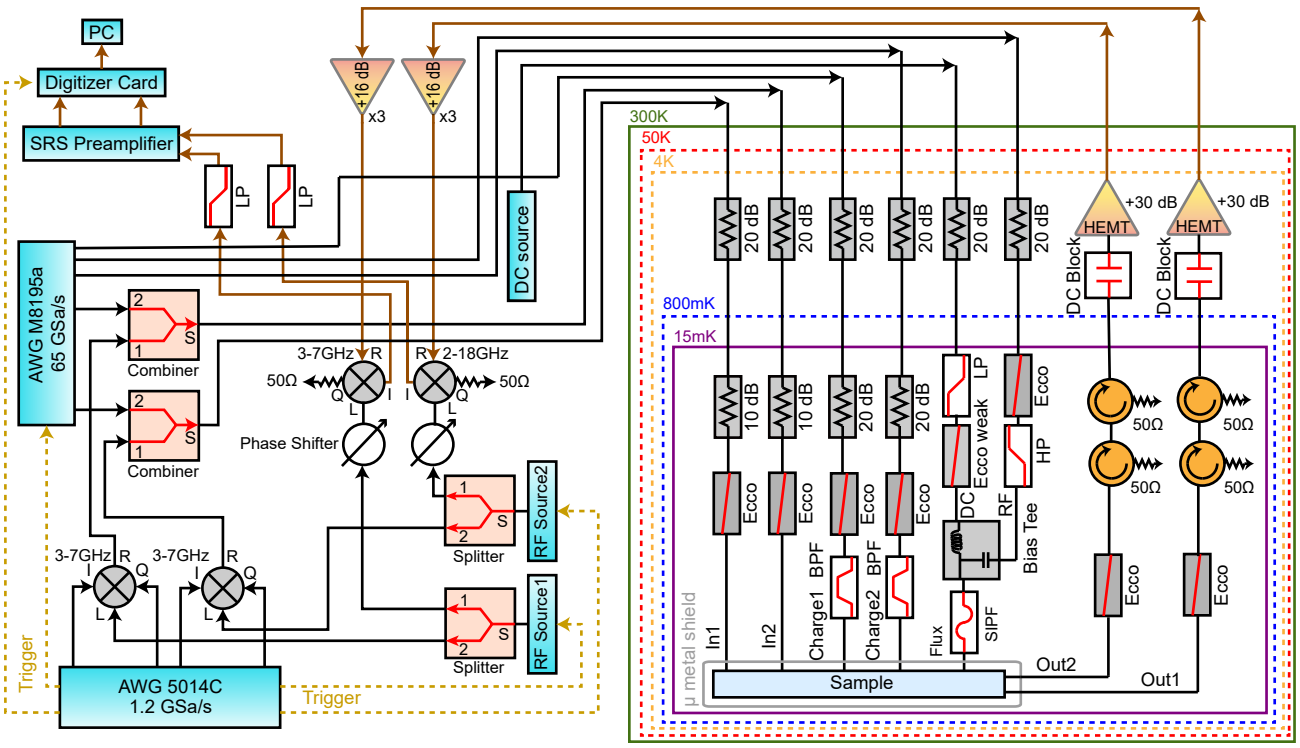

FIG. 14. Detailed cryogenic and room-temperature measurement setup.

ing 20 dB attenuation at 4 GHz; Charge_1 and Charge_2 lines have 20 dB attenuation, followed by a strong Eccosorb providing 20 dB attenuation at 4 GHz, and a band pass filter with pass band $3.9 - 4.8$ GHz. The DC Flux line has a low pass filter (DC $-$ 1.9 MHz), followed by a weak Eccosorb, and the RF Flux line passes through a weak Eccosorb first, followed by a high-pass filter (with a cut-off at 200 MHz). The DC and RF flux lines are combined with a Bias Tee, and then the signal passes through a stepped impedance Purcell filter (SIPF), which blocks the frequency band $2.5-5.5$ GHz corresponding to qutrit transition and readout resonator frequencies. The output signal goes through a weak Eccosorb, two circulators, a DC block, and is amplified with one LNF HEMT amplifier at 4K. The output signals are further amplified at room temperature and then demodulated with IQ mixers. The demodulated signals pass through low-pass filters (DC $-$ 250 MHz) and are amplified again using the SRS Preamplifier. The final signals are digitized with Alazar ATS 9870 (1 GSa/s) and analyzed in a computer.

[1] J. Preskill, Quantum computing in the nisq era and beyond, Quantum **2**, 79 (2018).

[2] F. Arute, K. Arya, R. Babbush, D. Bacon, J. C. Bardin, R. Barends, R. Biswas, S. Boixo, F. G. Brandao, D. A. Buell, *et al.*, Quantum supremacy using a programmable superconducting processor, Nature **574**, 505 (2019).

[3] Y. Wu, W.-S. Bao, S. Cao, F. Chen, M.-C. Chen, X. Chen, T.-H. Chung, H. Deng, Y. Du, D. Fan, M. Gong, C. Guo, C. Guo, S. Guo, L. Han, L. Hong, H.-L. Huang, Y.-H. Huo, L. Li, N. Li, S. Li, Y. Li, F. Liang, C. Lin, J. Lin, H. Qian, D. Qiao, H. Rong, H. Su, L. Sun, L. Wang, S. Wang, D. Wu, Y. Xu, K. Yan, W. Yang, Y. Yang, Y. Ye, J. Yin, C. Ying, J. Yu, C. Zha, C. Zhang, H. Zhang, K. Zhang, Y. Zhang, H. Zhao, Y. Zhao, L. Zhou, Q. Zhu, C.-Y. Lu, C.-Z. Peng, X. Zhu, and J.-W. Pan, Strong quantum computational advantage using a superconducting quantum processor, Phys. Rev. Lett. **127**, 180501 (2021).

[4] S. S. Bullock, D. P. O'Leary, and G. K. Brennen, Asymptotically optimal quantum circuits for d-level systems, Phys. Rev. Lett. **94**, 230502 (2005).

[5] T. C. Ralph, K. J. Resch, and A. Gilchrist, Efficient toffoli gates using qudits, Phys. Rev. A **75**, 022313 (2007).

[6] B. P. Lanyon, M. Barbieri, M. P. Almeida, T. Jennewein, T. C. Ralph, K. J. Resch, G. J. Pryde, J. L. O'brien, A. Gilchrist, and A. G. White, Simplifying quantum logic using higher-dimensional hilbert spaces, Nature Physics **5**, 134 (2009).

[7] Z. Gedik, I. A. Silva, B. Çakmak, G. Karpat, E. L. G. Vidoto, D. O. Soares-Pinto, E. R. deAzevedo, and F. F. Fanchini, Computational speed-up with a single qudit, Scientific reports **5**, 1 (2015).

[8] A. Nikolaeva, E. Kiktenko, and A. Fedorov, Efficient realization of quantum algorithms with qudits, arXiv

preprint arXiv:2111.04384 (2021).
[9] E. Kapit, Hardware-efficient and fully autonomous quantum error correction in superconducting circuits, Phys. Rev. Lett. **116**, 150501 (2016).
[10] S. Muralidharan, C.-L. Zou, L. Li, J. Wen, and L. Jiang, Overcoming erasure errors with multilevel systems, New Journal of Physics **19**, 013026 (2017).
[11] R. Majumdar, S. Basu, S. Ghosh, and S. Sur-Kolay, Quantum error-correcting code for ternary logic, Phys. Rev. A **97**, 052302 (2018).
[12] E. T. Campbell, Enhanced fault-tolerant quantum computing in d-level systems, Phys. Rev. Lett. **113**, 230501 (2014).
[13] E. T. Campbell, H. Anwar, and D. E. Browne, Magic-state distillation in all prime dimensions using quantum reed-muller codes, Phys. Rev. X **2**, 041021 (2012).
[14] A. S. Nikolaeva, E. O. Kiktenko, and A. K. Fedorov, Decomposing the generalized toffoli gate with qutrits, Phys. Rev. A **105**, 032621 (2022).
[15] A. Fedorov, L. Steffen, M. Baur, M. P. da Silva, and A. Wallraff, Implementation of a toffoli gate with superconducting circuits, Nature **481**, 170 (2012).
[16] P. Gokhale, J. M. Baker, C. Duckering, N. C. Brown, K. R. Brown, and F. T. Chong, Asymptotic improvements to quantum circuits via qutrits, in *Proceedings of the 46th International Symposium on Computer Architecture*, ISCA '19 (Association for Computing Machinery, New York, NY, USA, 2019) p. 554–566.
[17] E. Gustafson, Noise improvements in quantum simulations of sQED using qutrits, arXiv preprint arXiv:2201.04546 (2022).
[18] H. Bechmann-Pasquinucci and A. Peres, Quantum cryptography with 3-state systems, Phys. Rev. Lett. **85**, 3313 (2000).
[19] D. Bruß and C. Macchiavello, Optimal eavesdropping in cryptography with three-dimensional quantum states, Phys. Rev. Lett. **88**, 127901 (2002).
[20] A. Vaziri, G. Weihs, and A. Zeilinger, Experimental two-photon, three-dimensional entanglement for quantum communication, Phys. Rev. Lett. **89**, 240401 (2002).
[21] Y.-H. Luo, H.-S. Zhong, M. Erhard, X.-L. Wang, L.-C. Peng, M. Krenn, X. Jiang, L. Li, N.-L. Liu, C.-Y. Lu, A. Zeilinger, and J.-W. Pan, Quantum teleportation in high dimensions, Phys. Rev. Lett. **123**, 070505 (2019).
[22] X.-M. Hu, C. Zhang, B.-H. Liu, Y. Cai, X.-J. Ye, Y. Guo, W.-B. Xing, C.-X. Huang, Y.-F. Huang, C.-F. Li, and G.-C. Guo, Experimental high-dimensional quantum teleportation, Phys. Rev. Lett. **125**, 230501 (2020).
[23] M. Ringbauer, M. Meth, L. Postler, R. Stricker, R. Blatt, P. Schindler, and T. Monz, A universal qudit quantum processor with trapped ions, Nature Physics **18**, 1053 (2022).
[24] P. Hrmo, B. Wilhelm, L. Gerster, M. W. van Mourik, M. Huber, R. Blatt, P. Schindler, T. Monz, and M. Ringbauer, Native qudit entanglement in a trapped ion quantum processor, arXiv preprint arXiv:2206.04104 (2022).
[25] Y. Fu, W. Liu, X. Ye, Y. Wang, C. Zhang, C.-K. Duan, X. Rong, and J. Du, Experimental investigation of quantum correlations in a two-qutrit spin system, Phys. Rev. Lett. **129**, 100501 (2022).
[26] A. Morvan, V. V. Ramasesh, M. S. Blok, J. M. Kreikebaum, K. O'Brien, L. Chen, B. K. Mitchell, R. K. Naik, D. I. Santiago, and I. Siddiqi, Qutrit randomized benchmarking, Phys. Rev. Lett. **126**, 210504 (2021).
[27] N. Goss, A. Morvan, B. Marinelli, B. K. Mitchell, L. B. Nguyen, R. K. Nail, L. Chen, C. Jünger, J. M. Kreikebaum, D. I. Santiago, *et al.*, High-fidelity qutrit entangling gates for superconducting circuits, Nature Communications **13**, 7481 (2022).
[28] K. Luo, W. Huang, Z. Tao, L. Zhang, Y. Zhou, J. Chu, W. Liu, B. Wang, J. Cui, S. Liu, F. Yan, M.-H. Yung, Y. Chen, T. Yan, and D. Yu, Experimental realization of two qutrits gate with tunable coupling in superconducting circuits, Phys. Rev. Lett. **130**, 030603 (2023).
[29] A. Cervera-Lierta, M. Krenn, A. Aspuru-Guzik, and A. Galda, Experimental high-dimensional greenberger-horne-zeilinger entanglement with superconducting transmon qutrits, Phys. Rev. Applied **17**, 024062 (2022).
[30] A. Blais, A. L. Grimsmo, S. M. Girvin, and A. Wallraff, Circuit quantum electrodynamics, Rev. Mod. Phys. **93**, 025005 (2021).
[31] J. Koch, T. M. Yu, J. Gambetta, A. A. Houck, D. I. Schuster, J. Majer, A. Blais, M. H. Devoret, S. M. Girvin, and R. J. Schoelkopf, Charge-insensitive qubit design derived from the Cooper pair box, Physical Review A **76**, 042319 (2007).
[32] A. P. Place, L. V. Rodgers, P. Mundada, B. M. Smitham, M. Fitzpatrick, Z. Leng, A. Premkumar, J. Bryon, A. Vrajitoarea, S. Sussman, *et al.*, New material platform for superconducting transmon qubits with coherence times exceeding 0.3 milliseconds, Nature communications **12**, 1 (2021).
[33] C. Wang, X. Li, H. Xu, Z. Li, J. Wang, Z. Yang, Z. Mi, X. Liang, T. Su, C. Yang, *et al.*, Towards practical quantum computers: transmon qubit with a lifetime approaching 0.5 milliseconds, npj Quantum Information **8**, 1 (2022).
[34] R. Bianchetti, S. Filipp, M. Baur, J. M. Fink, C. Lang, L. Steffen, M. Boissonneault, A. Blais, and A. Wallraff, Control and tomography of a three level superconducting artificial atom, Phys. Rev. Lett. **105**, 223601 (2010).
[35] M. S. Blok, V. V. Ramasesh, T. Schuster, K. O'Brien, J. M. Kreikebaum, D. Dahlen, A. Morvan, B. Yoshida, N. Y. Yao, and I. Siddiqi, Quantum information scrambling on a superconducting qutrit processor, Phys. Rev. X **11**, 021010 (2021).
[36] Y. Lu, S. Chakram, N. Leung, N. Earnest, R. K. Naik, Z. Huang, P. Groszkowski, E. Kapit, J. Koch, and D. I. Schuster, Universal stabilization of a parametrically coupled qubit, Phys. Rev. Lett. **119**, 150502 (2017).
[37] T. Brown, E. Doucet, D. Ristè, G. Ribeill, K. Cicak, J. Aumentado, R. Simmonds, L. Govia, A. Kamal, and L. Ranzani, Trade off-free entanglement stabilization in a superconducting qutrit-qubit system, Nature communications **13**, 1 (2022).
[38] D. Deutsch and R. Jozsa, Rapid solution of problems by quantum computation, Proceedings of the Royal Society of London A: Mathematical, Physical and Engineering Sciences **439**, 553 (1992).
[39] Y. Wang, Z. Hu, B. C. Sanders, and S. Kais, Qudits and high-dimensional quantum computing, Frontiers in Physics **8**, 589504 (2020).
[40] E. Bernstein and U. Vazirani, Quantum complexity theory, SIAM Journal on Computing **26**, 1411 (1997).
[41] L. K. Grover, Quantum mechanics helps in searching for a needle in a haystack, Phys. Rev. Lett. **79**, 325 (1997).
[42] T. Roy, S. Hazra, S. Kundu, M. Chand, M. P. Patankar, and R. Vijay, Programmable superconducting processor

with native three-qubit gates, Phys. Rev. Applied **14**, 014072 (2020).
[43] M. J. Bremner, C. M. Dawson, J. L. Dodd, A. Gilchrist, A. W. Harrow, D. Mortimer, M. A. Nielsen, and T. J. Osborne, Practical scheme for quantum computation with any two-qubit entangling gate, Phys. Rev. Lett. **89**, 247902 (2002).
[44] C. Figgatt, D. Maslov, K. A. Landsman, N. M. Linke, S. Debnath, and C. Monroe, Complete 3-qubit grover search on a programmable quantum computer, Nature Communications **8**, 1918 (2017).
[45] A. Mandviwalla, K. Ohshiro, and B. Ji, Implementing grover's algorithm on the ibm quantum computers, in *2018 IEEE International Conference on Big Data (Big Data)* (2018) pp. 2531–2537.
[46] K. Zhang, P. Rao, K. Yu, H. Lim, and V. Korepin, Implementation of efficient quantum search algorithms on nisq computers, Quantum Information Processing **20**, 1 (2021).
[47] J. Chu, X. He, Y. Zhou, J. Yuan, L. Zhang, Q. Guo, Y. Hai, Z. Han, C.-K. Hu, W. Huang, *et al.*, Scalable algorithm simplification using quantum and logic, Nature Physics , 1 (2022).
[48] T. Roy, L. Jiang, and D. I. Schuster, Deterministic grover search with a restricted oracle, Phys. Rev. Research **4**, L022013 (2022).
[49] G. L. Long, Grover algorithm with zero theoretical failure rate, Phys. Rev. A **64**, 022307 (2001).
[50] M. Werninghaus, D. J. Egger, F. Roy, S. Machnes, F. K. Wilhelm, and S. Filipp, Leakage reduction in fast superconducting qubit gates via optimal control, npj Quantum Information **7**, 1 (2021).
[51] Z. Li, T. Roy, D. R. Perez, K.-H. Lee, E. Kapit, and D. I. Schuster, Autonomous error correction of a single logical qubit using two transmons (2023), arXiv:2302.06707 [quant-ph].
[52] Y. Lu, A. Maiti, J. W. O. Garmon, S. Ganjam, Y. Zhang, J. Claes, L. Frunzio, S. M. Girvin, and R. J. Schoelkopf, A high-fidelity microwave beamsplitter with a parity-protected converter (2023), arXiv:2303.00959 [quant-ph].
[53] M. Roth, M. Ganzhorn, N. Moll, S. Filipp, G. Salis, and S. Schmidt, Analysis of a parametrically driven exchange-type gate and a two-photon excitation gate between superconducting qubits, Phys. Rev. A **96**, 062323 (2017).
[54] M. Ganzhorn, G. Salis, D. J. Egger, A. Fuhrer, M. Mergenthaler, C. Müller, P. Müller, S. Paredes, M. Pechal, M. Werninghaus, and S. Filipp, Benchmarking the noise sensitivity of different parametric two-qubit gates in a single superconducting quantum computing platform, Phys. Rev. Research **2**, 033447 (2020).
[55] T. Roy, Z. Li, E. Kapit, and D. I. Schuster, Tomography in the presence of stray inter-qubit coupling, arXiv preprint arXiv:2103.13611 (2021).
[56] D. C. McKay, S. Filipp, A. Mezzacapo, E. Magesan, J. M. Chow, and J. M. Gambetta, Universal gate for fixed-frequency qubits via a tunable bus, Phys. Rev. Applied **6**, 064007 (2016).
[57] Y. Sung, L. Ding, J. Braumüller, A. Vepsäläinen, B. Kannan, M. Kjaergaard, A. Greene, G. O. Samach, C. McNally, D. Kim, A. Melville, B. M. Niedzielski, M. E. Schwartz, J. L. Yoder, T. P. Orlando, S. Gustavsson, and W. D. Oliver, Realization of high-fidelity cz and zz-free iswap gates with a tunable coupler, Phys. Rev. X **11**, 021058 (2021).
[58] E. A. Sete, N. Didier, A. Q. Chen, S. Kulshreshtha, R. Manenti, and S. Poletto, Parametric-resonance entangling gates with a tunable coupler, Phys. Rev. Applied **16**, 024050 (2021).